J. Fluid Mech. (2022), *vol*. 946, A4, doi:10.1017/jfm.2022.586

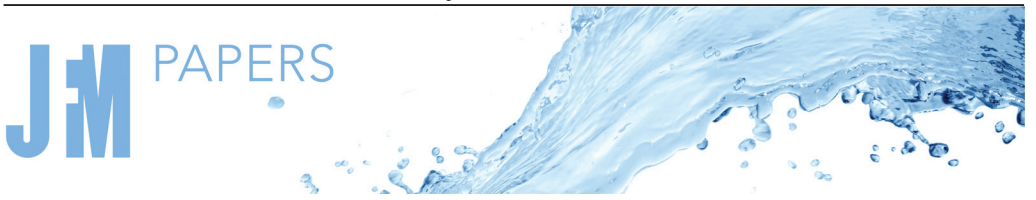

Two-fluid coaxial atomization in a high-pressure environment

Kee Onn Fong[1],†, **Xinzhi Xue**[1], **R. Osuna-Orozco**[1] **and A. Aliseda**[1]

[1]Department of Mechanical Engineering, University of Washington, Seattle, WA 98105, USA

(Received 14 February 2022; revised 23 May 2022; accepted 29 June 2022)

We study the dynamics of atomization of a liquid column by a coaxial gas flow with varying gas pressures. Specifically, we analyse how the gas density increase associated with elevated gas pressures in the ambient and co-flowing gas jet influences the liquid destabilization and breakup process, as well as the resulting droplet formation and dispersion. We present new experimental results for a coaxial liquid–gas atomizer operating in a high-pressure environment, with gas–liquid momentum ratio in the range $M = 5$–56 and pressurized gas densities $\rho_g/\rho_0 = 1$–5, where ρ_0 is the ambient gas density at standard conditions. High-speed shadowgraphy images are used to quantify the spatially and temporally varying liquid–gas interface in the spray near-field. Liquid core lengths, spreading angles and other spray metrics are presented, and the influence of gas density is identified from the comparison with atomization at atmospheric conditions. In the spray mid-field, phase Doppler interferometry is used in conjunction with laser Doppler velocimetry to quantify the droplet size and velocities, as well as their radial variations across the spray. Results show an increase in droplet size at elevated ambient pressures, when keeping the gas–liquid momentum ratio constant. Finally, we show that these observations are in line with predictions from the Kelvin–Helmholtz and Rayleigh–Taylor instabilities, both of which are relevant to the gas–liquid atomization process.

Key words: aerosols/atomization, gas/liquid flow, multiphase flow

1. Introduction

The production of a spray of atomized, small liquid droplets is highly desirable in many practical applications such as combustion, chemical dispersion, agricultural irrigation and surface deposition processes (Fansler & Parrish 2014). Fundamentally, liquid atomization is an important topic not just in terms of multi-phase flows but also in its numerous

† Email address for correspondence: kofong@uw.edu

applications, as discussed comprehensively in the reviews by Villermaux (2007) and Eggers & Villermaux (2008). Here, we describe a gas–liquid atomization set-up where a liquid column is surrounded by a coaxial gas flow, also known as air-blast atomization or gas-assisted liquid atomization; this set-up is reviewed comprehensively by Lasheras & Hopfinger (2000). Liquid atomization also poses challenges for numerical simulations due to the complex interfaces and having a wide range of scales, and these modelling challenges are the focus of a review by Gorokhovski & Herrmann (2008).

A liquid stream issuing into quiescent air will break up into droplets naturally due to the Rayleigh–Plateau instability (Lasheras & Hopfinger 2000). However, when the liquid stream is surrounded by a gas phase with a faster velocity, a Kelvin–Helmholtz instability arises at the liquid–gas interface due to the velocity difference between the two fluids. This creates a shear force that destabilizes the gas–liquid interface, giving rise to undulations along the liquid column. The competition between the destabilizing gas dynamic pressure and the capillary surface tension is represented by the Weber number, $We = \rho_g(U_g - U_l)^2 D_l/\sigma$, where D_l is the diameter of the liquid jet, and σ is the surface tension of the air–water interface (Marmottant & Villermaux 2004). Classical instability analysis shows that the Kelvin–Helmholtz instability is always unstable (Kundu, Cohen & Dowling 2015; Ng 2015). As the interface is deformed, the gas dynamic pressure acting on the deformed surface results in a radial transverse force that displaces the liquid column radially, with increasingly larger displacements as the liquid evolves downstream, appearing as a 'flapping' or helical instability (Eroglu, Chigier & Farago 1991; Chigier & Farago 1992; Matas & Cartellier 2006; Delon, Cartellier & Matas 2018). The liquid column atomizes eventually when it is oriented with the liquid–gas interface perpendicular to the airflow, and at low Weber numbers ($We < 100$; Chigier & Reitz 1996), the gas flow overcomes the liquid cohesive forces, such that it undergoes a bag-breakup process and forms multiple droplets. The whole process of breaking up the liquid column into droplets is termed the primary breakup, and the Kelvin–Helmholtz instability that gives rise to it is the primary instability. We note that this is a simplified view; the Kelvin–Helmholtz instability is by definition inviscid, and the initial gas and liquid flows are steady and of infinite thickness. In the context of liquid jet breakup, the effects of viscosity were studied and discussed in Matas (2015), the effects of finite thickness in Bozonnet *et al.* (2022), and the effects of unsteady gas turbulence in Matas *et al.* (2015) and Jiang & Ling (2021).

At high gaseous velocities corresponding to large Weber numbers ($We > 100$ in Chigier & Reitz 1996), the gas dynamic pressure is now much stronger than surface tension, and surface deformations associated with the primary Kelvin–Helmholtz instability grow more quickly and form ligaments out of the interface (Marmottant & Villermaux 2004; Villermaux 2007; Gorokhovski & Herrmann 2008). As these ligaments protrude past the boundary layer of the gas flow, the ligament surfaces are orthogonal to the high-speed gas flow and are suddenly exposed to a large acceleration due to air drag. Thus a secondary instability sets in, where the dynamic pressure of the air acts against the ligament surface, accelerating it strongly. This results in the formation of waves along the ligament length, as recognized by Varga, Lasheras & Hopfinger (2003) as being similar to an aero-driven Rayleigh–Taylor instability (Joseph, Belanger & Beavers 1999), where liquid droplets exposed suddenly to high gas velocities show undulations on the surface of the droplet. Like the Kelvin–Helmholtz instability, the Rayleigh–Taylor instability can also be studied in terms of its most unstable wavelength λ_{RT}, which grows at a maximum growth rate n (Aliseda *et al.* 2008; Ng 2015). The waves grow in amplitude, and ultimately the ligaments break into droplets, with the size of the droplets determined by the most unstable Rayleigh–Taylor wavelength λ_{RT}. The droplets formed are still subject to large gas

dynamic pressures, and may undergo secondary breakup into smaller droplets if the droplet Weber number is sufficiently large (Apte *et al.* 2003; Chen *et al.* 2017; Liu *et al.* 2021). Overall, the liquid breakup can be thought of as being driven by the transfer of momentum from the fast-flowing gas phase to the slower liquid phase, and can be characterized by a momentum ratio $M = \rho_g U_g^2/\rho_l U_l^2$, with subscripts g and l representing the gas and liquid phases, respectively (Lasheras & Hopfinger 2000). The aforementioned Weber number *We* also plays a role in determining the nature of the liquid column breakup, and the instabilities that come into play.

A practical goal is the control of the droplet size and dispersion, which is important for controlling liquid deposition and reaction rates for the aforementioned applications. Previous studies experimented with manipulating the gas flow, by means of injecting angular momentum into the co-flowing gas through off-axis inlets (Hopfinger & Lasheras 1996). By varying the ratio of the axial air velocity U_g and tangential air velocity U_t, Hopfinger & Lasheras (1996) observed an enhancement of the liquid breakup and broadening of the spray spreading angles past a critical ratio of $U_t/U_g \sim 0.4$ for momentum ratios $M > 10$. This is understood to be a manifestation of a vortex breakdown phenomenon when the radial pressure gradient induced by the angular velocity in the gas is above a stability threshold (Lasheras & Hopfinger 2000). Recent work in swirl-based spray control experimented with varying the angular component of the coaxial gas in time, through either open-loop forcing with a sinusoidal waveform (Machicoane *et al.* 2020), or closed-loop forcing with feedback control (Osuna-Orozco *et al.* 2019). Other studies in droplet size control involve either electrostatic fields (Osuna-Orozco *et al.* 2020) or pressure variations through acoustic forcing (Huck *et al.* 2021) around the coaxial jet.

These control strategies are proven to be successful in modulating key spray characteristics, such as the spreading angle and droplet size distribution, with the caveat that these studies are performed in standard temperature and pressure environments, which do not reflect the conditions in some applications, such as jet or rocket engines. In these environments, high temperature and pressure can change the spray characteristics, through a modulation of the initial gas–liquid breakup and atomization process, or the droplet transport and secondary breakup mechanisms downstream of the spray. Motivated by the importance of sprays in transportation applications, numerous studies have been done in fuel atomization with experiments that replicate high pressure and temperature conditions inside internal combustion engines (Naber & Siebers 1996; Pickett, Kook & Williams 2009; Pickett *et al.* 2010; Lubarsky *et al.* 2010). However, in these experiments the high operating temperatures are linked inextricably to changes in the properties of the gas and liquid phases, including dynamic viscosities (Lo, Carroll & Stiel 1966) and the gas–liquid interfacial surface tension (Vargaftik, Volkov & Voljak 1983), which in turn affects the mechanisms related to droplet formation. Other efforts have focused on elevated pressures, but keeping the standard temperature, to investigate the effect of higher ambient air pressures (and densities) on the mechanics of spray dispersion. These studies include near-nozzle dispersion of diesel spray injectors using X-ray radiography techniques (Kastengren *et al.* 2009), and shadowgraphy measurements of a spray in cross-flow produced by a coaxial atomizer (Leong, McDonell & Samuelsen 2001). While these studies provide visualizations and important information on liquid column breakup at elevated pressures, other essential details are lacking, such as the actual diameters of the liquid droplets formed.

The present experimental study employs a set-up with a coaxial atomizer, described extensively in Machicoane *et al.* (2020) and Huck *et al.* (2022), where a liquid jet issues with co-flowing air into a chamber with quiescent air with varying ambient pressures but

constant, room temperature conditions. As mentioned before, this is necessary in order to decouple the effects of pressure and temperature on the liquid and gas properties, and allows us to study the influence of gas pressure (and density) on the mechanics of atomization of the liquid phase. The paper is organized as follows. In § 2, we describe the experimental facility for high-pressure coaxial gas–liquid atomization and the parameter space explored. In § 3, we describe the experimental technique employed to study the near-field, and present results including the intact liquid length, spreading angles and dominant frequencies in the spray. In § 4, we describe the droplet measurement technique used in the mid-field, and present radial profiles of the droplet characteristic diameters and velocities, as well as the integral variables in the jet, including liquid recovery rates and momentum fluxes in the gas and liquid phases, and the slip between them. In § 5, we discuss the results in the context of the effect of high pressures on the instabilities governing the atomization process. Finally, in § 6, we draw conclusions and offer an outlook for control strategies.

2. Experimental method

2.1. *Description of the high-pressure atomization facility*

A specialized custom-built pressurized coaxial jet facility is shown in figure 1, with the capability to change the ambient air pressure surrounding the coaxial jet from 1 to 5 times the standard atmospheric pressure. This is achieved by enclosing the coaxial nozzle in a 190 litre stainless steel tank, and feeding the coaxial gas jet with highly pressurized air. Increasing ambient air pressure results in higher air density ρ_g, which we report as ρ_g/ρ_0, where $\rho_0 = 1.2$ kg m^{-3} is the ambient gas density at standard conditions. The value of ρ_g can be approximated (neglecting temperature changes as a slow isothermal process) by the ideal gas law $\rho_g = P_g m_g/RT$, where P_g is the air pressure in units of Pa, $m_g = 28.97$ g mol^{-1} is the molar mass of air, $R = 8.3145$ m^3 Pa K^{-1} mol^{-1} is the universal gas constant, and T is the air temperature in kelvins (the term 'air' refers to the gas phase for the rest of the paper).

The two-fluid coaxial atomizer that produces the spray is shown in figure 1(*c*), which has been described extensively in Machicoane *et al.* (2019, 2020) and Huck *et al.* (2022). Briefly, the liquid and gas jets flow continuously during operation, with liquid jet diameter $d_l = 2$ mm and annular gas jet diameter $d_g = 10$ mm. Liquid and air flow rates are regulated to be steady in time by proportional integral derivative (PID) controls in the flow loop, with user inputs mediated through a National Instruments LabView program. An additional PID circuit is used to regulate the ambient air pressure, which is required as varying atomizing air flow rates will increase the ambient air pressure inside the facility if the air injected is not allowed to exit at the correct rate. Glass imaging windows are built in to enable visible light imaging and laser Doppler velocimetry (LDV) measurements. Due to the fixed position of the glass windows, the nozzle is placed on a two-axis traverse system to enable measurements at different locations inside the spray. More details on the facility, including the construction process, are given in Burtnett *et al.* (2021).

2.2. *Parameter range studied*

The experimental parameters are listed in table 1. We employ purified water for the liquid phase, with the liquid flow rates (and Reynolds number) kept constant throughout the full parameter range for which experiments were conducted. The co-flowing air is controlled within a range of atomizing air flow rates characterized by the momentum ratio

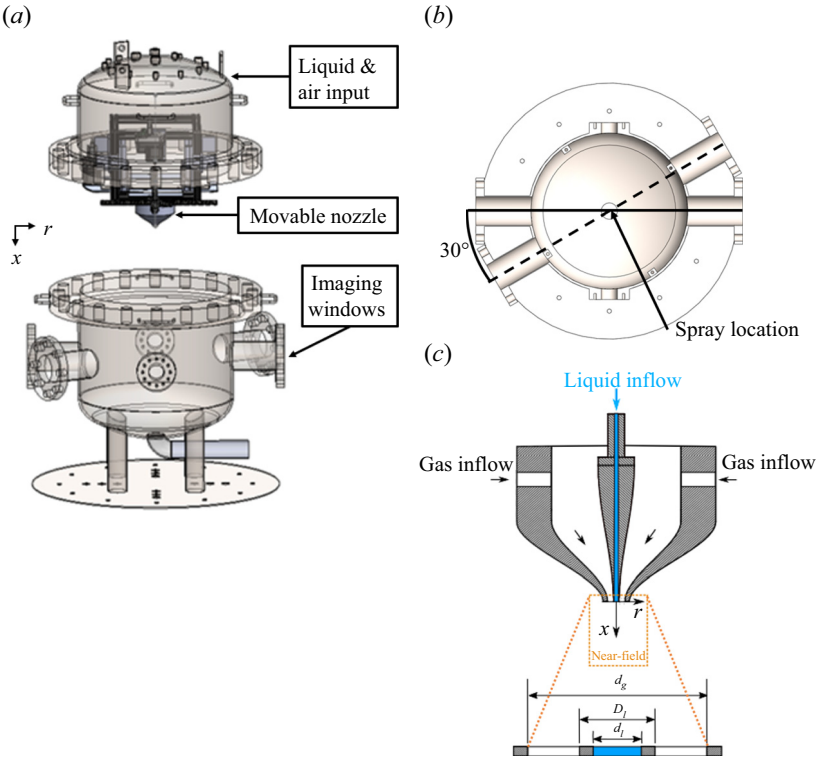

Figure 1. Schematic representation of the pressurized coaxial jet facility: (*a*) front view, and (*b*) top view, including the angles between the four viewing windows. Panel (*c*) is an inset of the movable nozzle, showing the inner and outer diameters of the liquid inlet, d_l and D_l, as well as the inner diameter of the air inlet, d_g.

Air nozzle diameter, d_g (mm)	10
Air dynamic viscosity, μ_g (kg m^{-1} s^{-1})	1.8×10^{-5}
Ambient air temperature, T (°C)	20
Ambient air density, ρ_0 (kg m^{-3})	1.2
Liquid nozzle diameter, d_l (mm)	2
Liquid density, ρ_l (kg m^{-3})	1000
Liquid kinematic viscosity, ν_l (m^2 s^{-1})	9.0×10^{-7}
Liquid Reynolds number, Re_l	1200
Air–liquid surface tension, σ (mN m^{-1})	73
Momentum ratio, M	5–56
Gas density ratio, ρ_g/ρ_0	1–5
Liquid–gas density ratio, ρ_g/ρ_l	160–820
Liquid Weber number, We	37–430

Table 1. Main physical parameters characterizing the experiments.

$M = \rho_g U_g^2/\rho_l U_l^2$, which is the ratio of the gas dynamic pressure to that of the liquid. Previous experiments described in Lasheras, Villermaux & Hopfinger (1998) and Lasheras & Hopfinger (2000) found that primarily, the momentum ratio dictates the atomization behaviour of the liquid jet, as confirmed for this set-up under atmospheric conditions

(Machicoane *et al.* 2020). The momentum ratio dictates the different liquid breakup modes. When the co-flowing gas velocity is low (low M, between 1 and 10), the liquid column undergoes mainly a bag-like breakup process, whereas in fast co-flowing air (high M, greater than 10), the liquid column is 'stripped' at its surface and forms ligaments, which then break up via a Rayleigh–Taylor instability (Aliseda *et al.* 2008). Swirl, or angular momentum in the air jet, as described for atomization control experiments in previous studies, e.g. Machicoane *et al.* (2019, 2020), is not studied here.

Another important parameter is the liquid–gas density ratio ρ_g/ρ_l, which varies as the ambient air pressure is increased. Specifically, as the air density ρ_g/ρ_0 increases from 1 to 5, ρ_g/ρ_l decreases from 820 to 160; i.e. at the highest air pressure, the water is only approximately 100 times denser than the ambient (and co-flowing) air. Finally, the liquid Weber number $We = \rho_g(U_g - U_l)^2 d_l/\sigma$, which also influences the liquid breakup process, ranges from 30 to 400. In summary, two independent parameters, the momentum ratio M and the gas density ratio ρ_g/ρ_0, result in a total of 20 different experimental conditions in which the near-field dynamics of the coaxial jet atomization, as well as the mid-field droplet size and velocity profiles, are studied. Intrinsic liquid and gas properties, such as the dynamic viscosity and air–water surface tension σ, are dependent mainly on temperature and are largely unaffected by pressure (Lo *et al.* 1966; Vargaftik *et al.* 1983). The isothermal set-up ensures that temperature does not change significantly between experiments, and thus does not affect these properties. All results represent the effect of the change in air density only.

3. Experiments in the spray near-field

3.1. *High-speed shadowgraphy imaging*

The near-field of the spray is the region where primary breakup of the liquid jet occurs, and we define it in this study as $0 < x/d_g < 9$, in the axial direction starting at the nozzle. In the near-field, the small time scales associated with the liquid atomization process require the use of high-speed imaging to observe the flow with sufficient temporal resolution. We obtain high-speed videos of the jet using a shadowgraphy method (figure 2), with a light source and an imaging system placed opposite each other, with the spray situated in between, such that the liquid column appears as a dark region against the light source. The illumination system comprises a DC LED source (Veritas Constellation 120E) with a diffuser (Westcott Scrim Jim) to ensure a uniform light background, and the imaging system is a high-speed camera (Phantom v12) paired with a Nikon 180 mm f/4 lens and a 2× teleconverter, placed 1 m away from the nozzle. This results in a field of view 30 mm × 30 mm, and spatial resolution 37 μm px^{-1} (magnification approximately 0.6). The image acquisition frame rate is 10 000 frames per second, resulting in total acquisition time 1.5 s, with 3 μs exposure time for each frame.

After the images are obtained, further processing is required in order to eliminate biases from, for example, uneven lighting effects, as illustrated in figure 3. These procedures are similar to those described in Machicoane *et al.* (2020). First, a background subtraction procedure is performed to remove the vignetting effect of the optics. Next, a normalization is applied on each frame, dividing the brightness values throughout the field by the value of the brightest pixel, such that the values of the dimmest and the brightest pixels are 0 and 1, respectively. A binarizing procedure follows, where regions having intensity values >0.5 are considered as the liquid phase being present, and are assigned binary value 1, and values below >0.5 are assigned value 0. We note that this imaging and thresholding method informs only the presence or absence of liquid along the line of sight, and not the

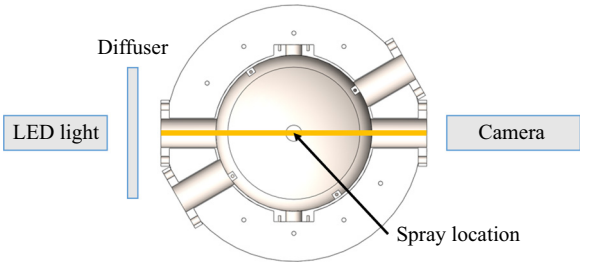

Figure 2. Schematic of the high-speed shadowgraphy set-up.

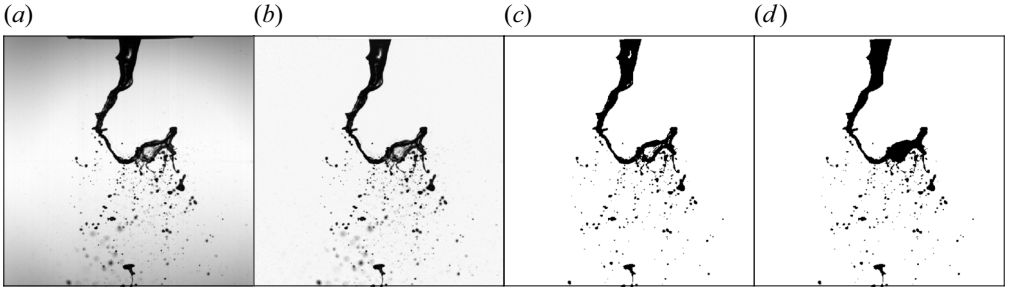

Figure 3. (*a*) Original image, (*b*) image after background subtraction, (*c*) image after normalization and binarization, and (*d*) final image after filling in gaps due to lighting conditions.

amount of liquid present throughout the spray. Finally, to correct for reflections of the light source on the liquid core, a filling procedure is used to fill in gaps in the binarized images, where regions with intensities below the threshold but with perimeters above the threshold intensity are adjusted such that these regions are also considered as being occupied by the liquid phase.

We obtain high-speed shadowgraphy videos of the near-field spray for four different momentum ratios M, and five different air density ratios ρ_g/ρ_0. Figure 4 shows representative images of the spray at the various conditions. Qualitatively, one can already infer that the momentum ratio M dominates the near-field breakup dynamics. An increase of M from 5 to 25 (which corresponds to the liquid Weber number We increasing from 37 to 189 at $\rho_g/\rho_0 = 1$, and from 35 to 186 at $\rho_g/\rho_0 = 5$) induces the transition from a bag-breakup regime to a ligament-breakup regime (Chigier & Reitz 1996). Further increases in the momentum ratio result in the liquid column becoming shorter, similar to observations in Machicoane *et al.* (2020) and Huck *et al.* (2022). In contrast, the effect of increasing the air density ratio ρ_g/ρ_0 is not apparent immediately in the instantaneous images. Statistical analysis of the videos is required to elucidate the effects of increased ambient air pressure on a spray with similar momentum ratios, as shown in the next subsection.

3.2. *Core length statistics*

For each image obtained, we extract the intact liquid core length, defined as the axial length of a continuous region where liquid is present, as shown in figure 5(*a*). Doing this over the full acquisition sequence results in a time-resolved liquid core length signal $L_B(t)$. With total acquisition time 1.5 s, $L_B(t)$ converges to an average value $\langle L_B \rangle$

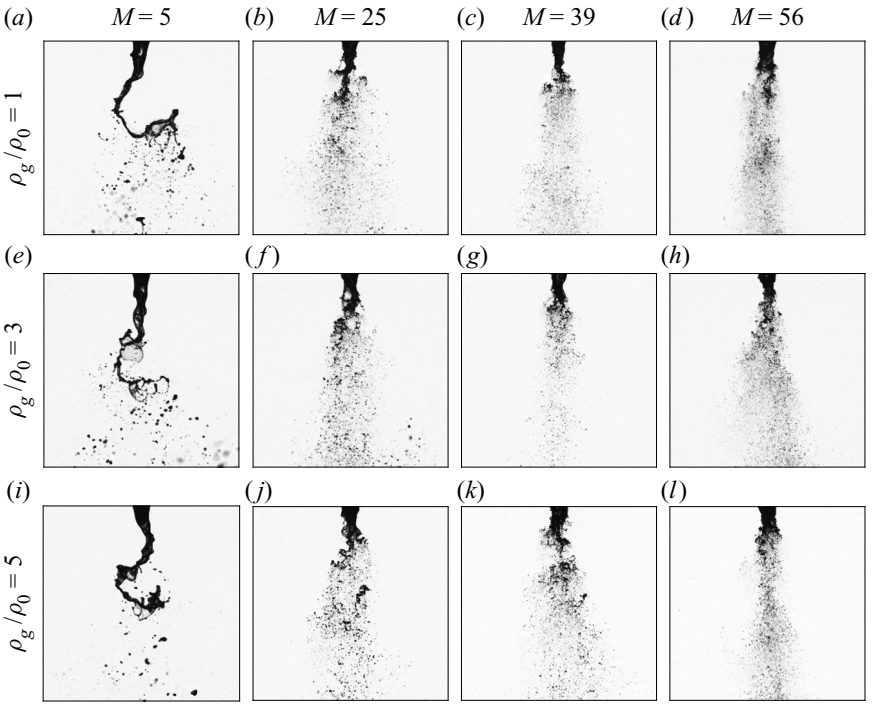

Figure 4. Instantaneous images of the spray at different momentum ratios M, increasing from (a,e,i) to (d,h,l), and different air density ratios ρ_p/ρ_g, increasing from (a–d) to (i–l).

(figure 5c) such that the mean and r.m.s liquid core lengths can be compared for different momentum ratios and ambient pressures. Error bars associated with the data points represent statistical uncertainties, calculated based on 95 % confidence intervals and using the random uncertainty of the time-resolved signal (Bendat & Piersol 2011).

As shown in figure 6(a), the average liquid core length trends mainly with momentum ratio, with a reciprocal relationship also observed in Machicoane *et al.* (2020). Increasing the air density results in a subtle but measurable increase in the liquid core length, for all momentum ratio cases. The r.m.s. fluctuations of the liquid core length, L_B' are shown in figure 6(b). The r.m.s. fluctuations decrease mainly with increasing momentum ratio, however, the trend of the r.m.s. fluctuations with increasing air density is less pronounced. Considering that higher momentum ratios ($M > 25$) result in more complete atomization, the r.m.s. fluctuations appear to decrease with higher air density, at these high momentum ratios. For the lower momentum ratios ($M \leq 25$), however, the r.m.s. fluctuation change with air density is either positive or flat (no correlation). In any case, the momentum ratio still dictates the mean and r.m.s values of the liquid intact core length.

We also leverage the time-resolved measurement to compute the autocorrelation time of $L_B(t)$, or the time required for fluctuations in the liquid core length to become uncorrelated, which informs a characteristic time scale of the liquid core length. The autocorrelation is defined as

$$C_{L_B}(\Delta t) = \frac{\langle L_B'(t)\, L_B'(t+\Delta t)\rangle}{\langle L_B'(t)^2\rangle}, \tag{3.1}$$

where $L_B' = L_B - \langle L_B\rangle$ is the fluctuation of the intact liquid core length about the mean. The point where the value of C_{L_B} decays to 1/e (as illustrated in figure 5d) is taken as the

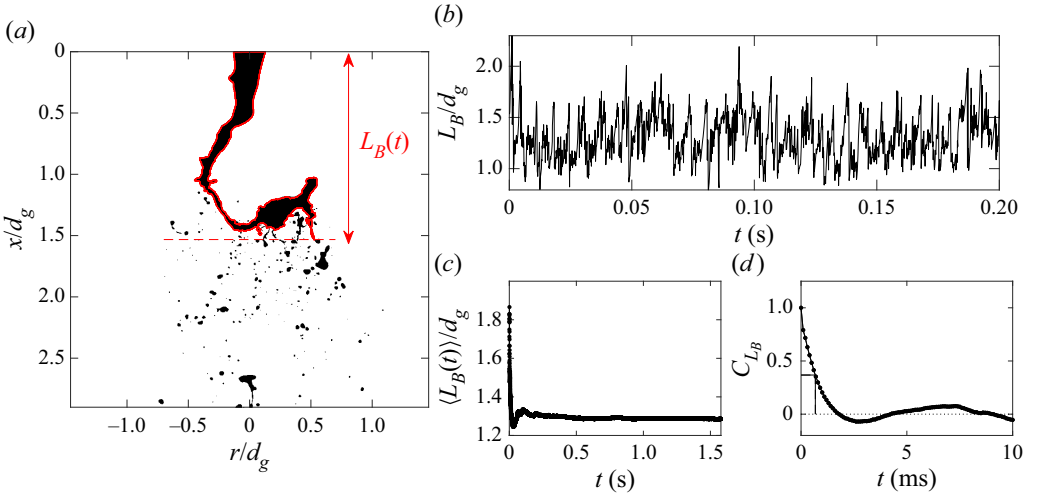

Figure 5. (*a*) Instantaneous image of the spray showing the liquid intact core length L_B for case $M = 5$, $\rho_g/\rho_0 = 1$. (*b*) Plot showing a time series of the evolution of L_B in time, for the same case $M = 5$, $\rho_g/\rho_0 = 1$. (*c*) Convergence plot of the liquid intact core length. (*d*) Autocorrelation example of the liquid core length.

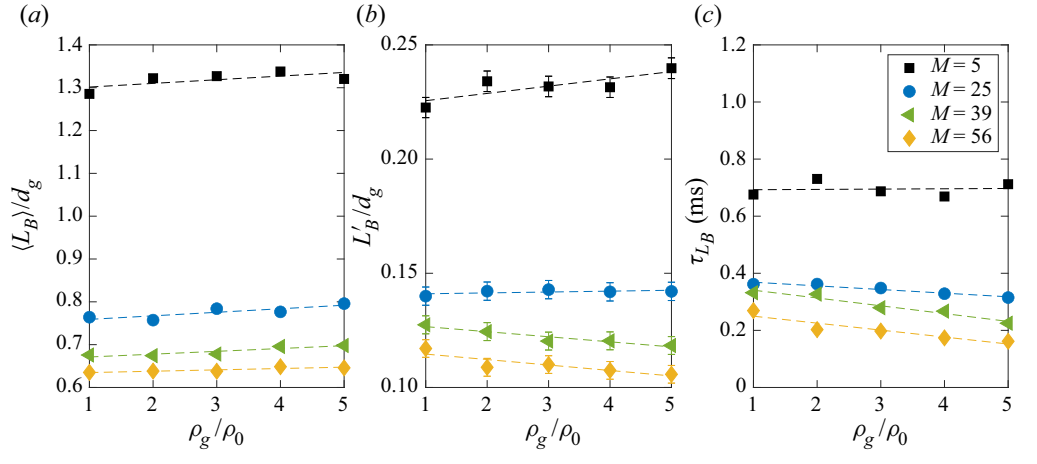

Figure 6. Liquid core length characteristics as functions of air density ratio ρ_g/ρ_0. (*a*) Mean liquid core length $\langle L_B\rangle/d_g$. (*b*) R.m.s. fluctuation L'_B/d_g. (*c*) Characteristic time scale derived from the autocorrelation τ_{L_B}. Symbols represent different momentum ratios as indicated in the legend in (*c*). Dashed lines represent a linear fit of the data points for each momentum ratio. Where not visible, error bars associated with the data points are smaller than the data symbol itself.

characteristic correlation time of the liquid core, τ_{L_B}. Note that in the autocorrelation plot, C_{L_B} also crosses the zero point, showing an anti-correlation where a long core length is usually followed by a short core length after 2 ms (and vice versa).

In figure 6(*c*), we compare the characteristic time scale of the core length, τ_{L_B}, for different momentum ratios and air densities. Similar to previous results, the characteristic time scale appears to be determined mainly by the momentum ratio, with a negative effect of increasing air density. This is also true only for the higher momentum ratios ($M \geq 25$); for the lowest momentum ratios where the atomization regime is different ($M = 5$), there is no noticeable correlation of τ_{L_B} with increasing air density.

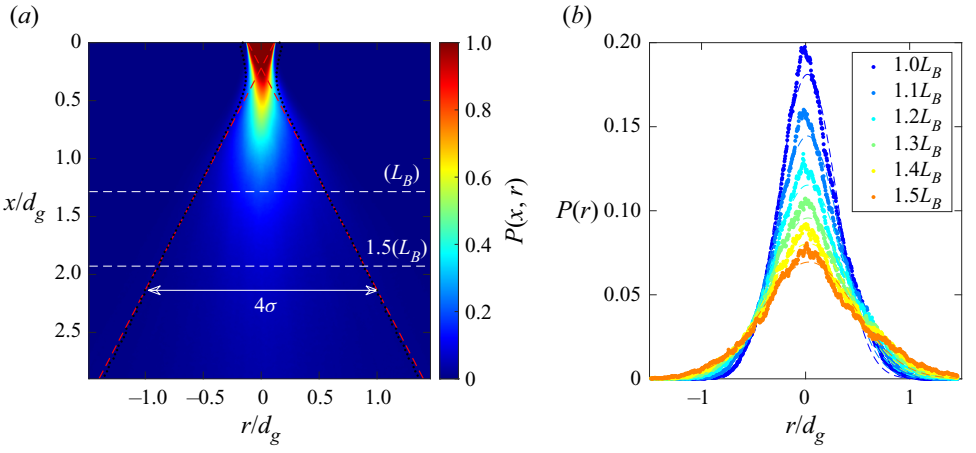

Figure 7. (*a*) Probability of liquid presence, $P(x, r)$, averaged over the entire image set (from the binarized shadowgraph images). The location of the spray edge (delineated by red dashes at angle θ, with the virtual origin x_0) is defined as $r/d_g = \pm 2$ s.d.. The axial locations of $\langle L_B \rangle$ and $\langle 1.5L_B \rangle$ are marked in white dashes. (*b*) Profiles of axial slices showing the Gaussian distribution of the liquid presence probabilities.

3.3. *Spreading angle and virtual origin*

From the binarized images shown in figure 3(*d*), an ensemble average can also be conducted for the full image sequences. The resulting liquid probability field (figure 7*a*) has values ranging from 0 to 1, corresponding to regions where liquid is never present throughout the experiment, to regions where liquid is always present, respectively. Following Machicoane *et al.* (2020), we use the time-averaged liquid probability field to derive the spray spreading angle, using the notion that for axial distances of 1–1.5 times the liquid bulk length, i.e. $L_B < x < 1.5L_B$, an axial slice of the field yields a Gaussian profile (figure 7*b*), and it being true for the different axial distances implies self-similarity. Leveraging this, the standard deviation (s.d.) of the Gaussian is calculated for each axial distance, and the location of $r/d_g = \pm 2$ s.d. is plotted to define the spray edge. This is followed by fitting a line through the points representing the spray edge for $L_B < x < 1.5L_B$ on both sides. The angle that the two lines subtends is the spreading angle θ, whereas the axial location where the two lines meet is the virtual origin x_0.

Figure 8(*a*) shows, for the different momentum ratios, that generally, the spray spreading angle decreases with increasing air density. The effect is more pronounced in the higher momentum ratio cases, where more complete atomization results in a more unambiguous decrease in the spreading angle corresponding to a narrowing of the jet. Similar trends can be inferred from figure 8(*b*), which shows that the axial value of the virtual origin decreases with increasing air density (negative values show that the location of the spray virtual origin is above the imaging field, i.e. inside the nozzle). As with the liquid core length, the values of the spray spreading angle and the virtual origin are dominated mainly by the momentum ratio (Machicoane *et al.* 2020). The spreading angle is a time-averaged manifestation of the Kelvin–Helmholtz instability, which will be shown to have a characteristic wavelength and a corresponding growth rate that is modulated with increasing air density. This is reflected in the overall spray characteristics as a narrowing of the jet and an upstream shift of the jet virtual origin.

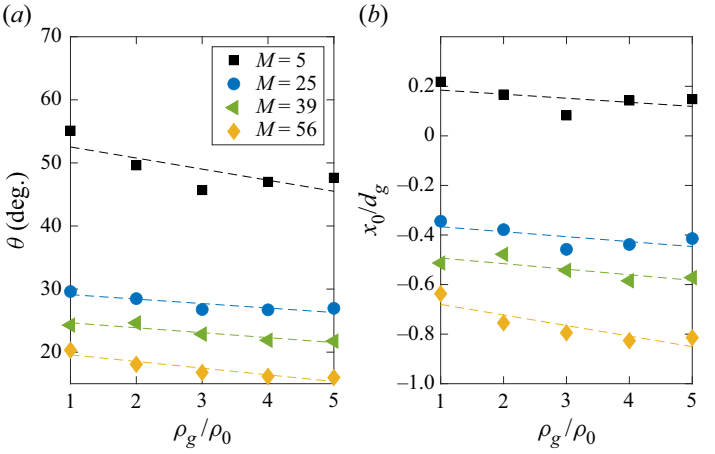

Figure 8. Spray characteristics, as functions of air density ratio ρ_g/ρ_0, for (*a*) the spreading angle θ, and (*b*) the virtual origin x_0. Symbols represent different momentum ratios, as indicated in the legend in (*a*). When not visible, the error bars have sizes similar to or smaller than the data point symbol.

3.4. *Frequency analysis*

We also leverage the measurements' time resolution to compute the characteristic frequencies associated with the spray. In Machicoane *et al.* (2020), a power spectral density (PSD) analysis is performed on the time-resolved liquid intact core length $L_B(t)$ signal, showing characteristic frequencies of the liquid bulk length that change with the swirl ratio *SR*. In our case, since the effect of pressure on the liquid core length is more subtle, we opted to perform the PSD analysis in a spatially resolved manner, i.e. directly on the time-resolved binarized liquid presence field instead.

For each radial location r, an axial average of the binarized liquid presence field (for example, shown in figure 3(*d*)) is taken at axial distances $0.75 < x/\langle L_B \rangle < 1.25$, where $\langle L_B \rangle$ is the mean liquid bulk length for each case. This is repeated for each time step, resulting in an axial-averaged, time-resolved liquid presence signal $P(t)$ on which the PSD analysis is performed. The results of the PSD analysis are plotted in figure 9, with the radial location r represented in the x-axis, the frequencies in the y-axis, and the PSD magnitudes in the colour axis. The dominant frequencies in the PSD colour contours are the frequencies for which the liquid phase appears and disappears over time due to breakup. This spatially resolved colour contours of the PSD for each radial location allows a clearer visualization of the characteristic frequencies of the liquid column breakup.

At a low momentum ratio $M = 5$, the magnitudes of the PSD in the colour contours show a peak value at around 150 Hz, which is sustained across the radial span of the jet, as shown in figure 9(*a*). This value is concurrent with the PSD analysis of the liquid core length signal in Machicoane *et al.* (2020), as well as a similar spatially resolved PSD analysis in Delon *et al.* (2018). An increase in the momentum ratio (figures 9*a–d*) results in the spray exhibiting a higher characteristic frequency in its liquid column breakup. This can be interpreted as an effect of the narrowing of the spray spreading angle at higher momentum ratios – when the spray is narrower, more liquid breakup events occur over the same time period in a more confined spatial region, as the liquid flow rate is unchanged. This results in an observed increase in the frequencies characterizing the liquid presence in the spray. Figure 9 also exhibits a shift in the spatially resolved PSD plots to peak only at the edges of the liquid column, indicating a transition from the bag-breakup regime in

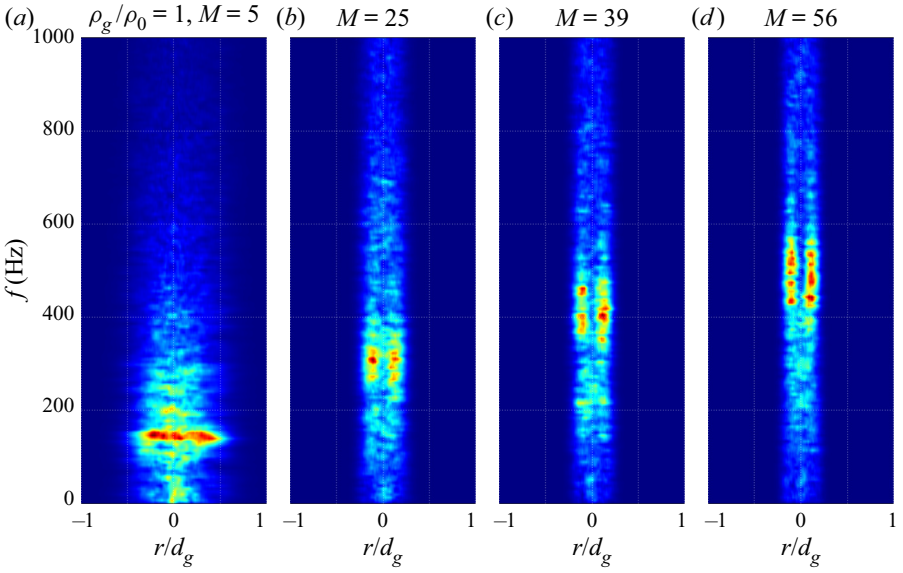

Figure 9. Colour contours for the PSD of the liquid presence field, with the y-axis indicating frequencies and x-axis indicating radial distances. The air density ratio is $\rho_g/\rho_0 = 1$, and momentum ratio M increases from (*a*) to (*d*).

$M = 5$ (corresponding to $We = 37$), where the bag-breakup process occurs across the radial span of the jet, to the more energetic ligament-breakup regime from $M = 25$ onwards (corresponding to $We > 180$), where liquid breakup occurs on ligaments surrounding the main jet. The findings for this transition align well with previous studies by Chigier & Reitz (1996), where the bag–ligament breakup transition occurs at $We \sim 100$.

Figure 10 shows the results of the PSD analysis performed on the same momentum ratios but for a higher air density ratio ($\rho_g/\rho_0 = 5$). Compared to figure 9, we observe similar spatial patterns in the PSD colour contours, but higher characteristic frequencies in the liquid breakup with higher air density. This indicates that the increase in air density produces an effect similar to that from increasing the momentum ratio, i.e. reducing the spray spreading angle and producing more energetic liquid breakup. However, the similar spatial patterns also indicate that the breakup regimes (bag-breakup transitioning to ligament-formation) are similar between low and high densities, and are well defined by M and We. This observation, combined with the previous observations of elongation of the mean intact liquid core length (figure 6*a*) and the narrowing of the spray (figure 8*a*), suggests that at high air densities, the momentum transfer from the gas phase to the liquid phase is enhanced, even when the momentum ratio is maintained.

4. Experiments in the spray mid-field

4.1. *Phase Doppler interferometry and laser Doppler velocimetry*

The mid-field of the spray is defined as the region with axial distances $x/d_g \geq 9$. Physically, this represents the region where the liquid jet has broken up into droplets that are advected downstream and may undergo secondary breakup if they are unstable, i.e. their aerodynamic Weber number is larger than a critical value, usually $We_{crit} > 4$ (Michaelides, Crowe & Schwarzkopf 2016; Chen *et al.* 2017). Quantities of interest in

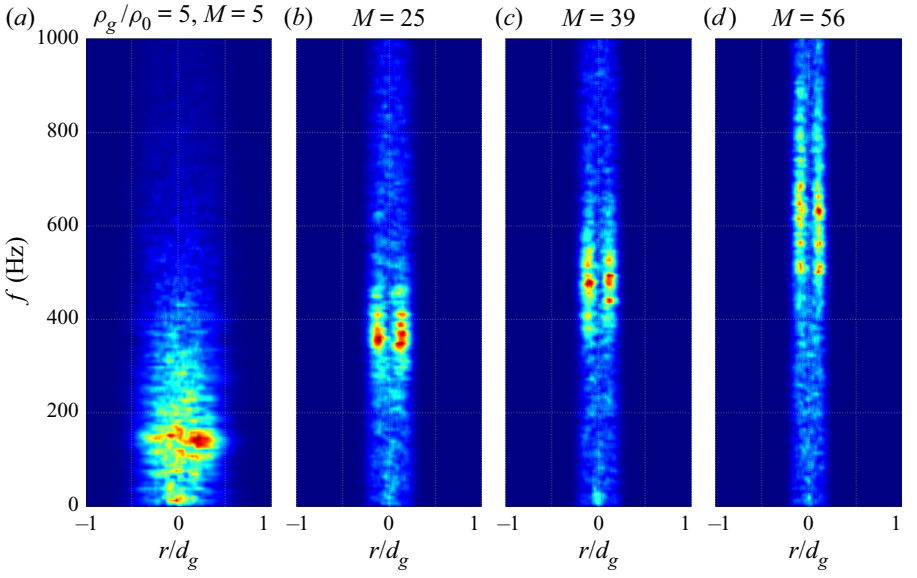

Figure 10. Colour contours for the PSD of the liquid presence field, with the y-axis indicating frequencies and x-axis indicating radial distances. The air density ratio is $\rho_g/\rho_0 = 5$, and momentum ratio M increases from (a) to (d).

this region include the droplet velocities and diameters. Coalescence of droplets in the mid-field could also be considered, as was done by Lasheras *et al.* (1998).

In this study, we conduct point measurements of the droplet diameters and velocities using phase Doppler interferometry (PDI) and LDV. This is done with a TSI LDV/PDI system (FSA4000 Signal Processor, PDM1000 Photo Detector Module) using forward scattering in the first refraction mode, where the transmitter and receiver are aligned at angle 30° as shown in figure 11. Droplet velocities are measured in the axial and radial directions, and droplet diameters are derived from intensity values of the scattered light signal (Albrecht *et al.* 2013). These point measurements are repeated along the radial direction to obtain the droplet diameter and velocity profiles across the spray. As mentioned previously, the viewing windows on the pressurized vessel are fixed, so the nozzle is traversed across the LDV/PDI probe volume to collect measurements across the different radial locations of the spray.

4.2. *Droplet size distributions*

PDI results are reported in the form of radial profiles of mean diameter in figures 12 and 13. Figure 12 shows the arithmetic mean diameter d_{10}, whereas figure 13 shows the Sauter mean diameter d_{32}, which can be interpreted as a mean diameter weighted by the volume to surface area ratio. The generalized form of the various diameters reported can be summarized as

$$d_{m,n} = \left(\frac{\sum d_d^m}{\sum d_d^n} \right)^{1/(m-n)}, \tag{4.1}$$

where d_d represents the absolute diameter of the individual droplet measured at the sampling point. In each figure, the results are plotted in panels (a–c) for the three

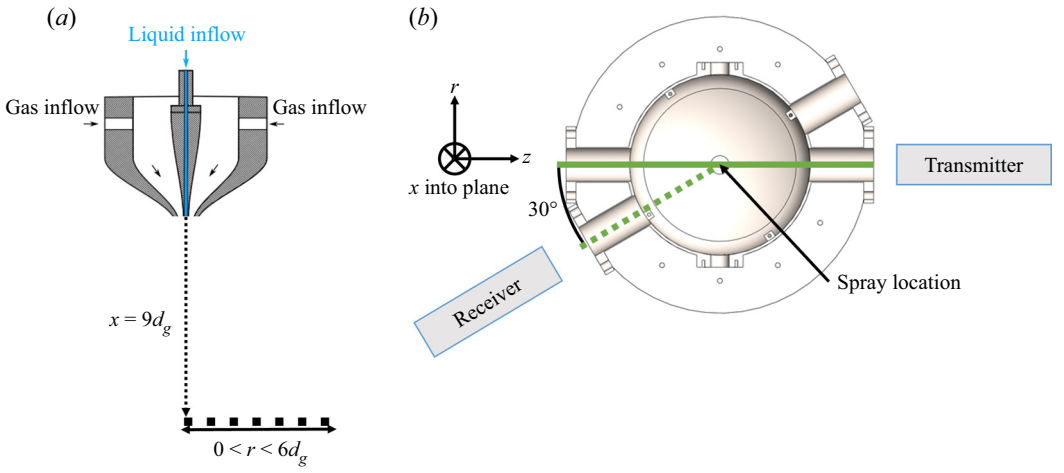

Figure 11. LDV/PDI system set-up to study the spray mid-field under high ambient pressures/densities. (*a*) Front view of the set-up, including the axial distance from the nozzle and the radial span of the sampling locations. (*b*) Top view of the set-up, including the orientation of the transmitter and receiver modules.

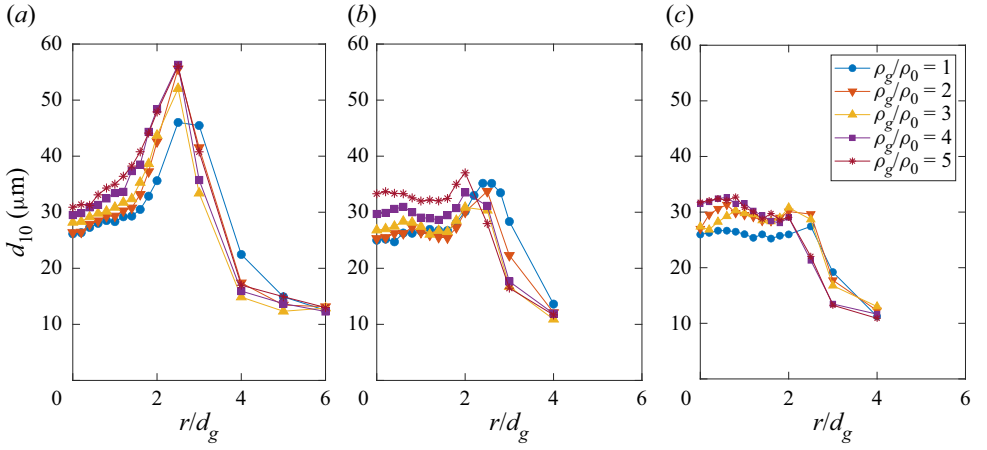

Figure 12. Radial profiles of the arithmetic mean droplet diameter d_{10} for the three momentum ratios: (*a*) $M = 25$, (*b*) $M = 39$, and (*c*) $M = 56$. Symbols indicate different air density ratios corresponding to the legend in (*c*).

momentum ratios $M = 25, 39, 56$, and the symbols representing five different air density ratios, $\rho_g/\rho_0 = 1$–5.

Trends in the radial profile of the droplet diameters, for both the arithmetic mean (figure 12) and the Sauter mean (figure 13), are dominated by the momentum ratio M. As M increases from left to right in figures 12 and 13, the shapes of the droplet diameter profiles change from concave to flat. This is an effect of the spray behaviour transitioning past a critical value of the momentum ratio, $M_C \sim 50$ (Lasheras & Hopfinger 2000). Physically, Huck *et al.* (2022) described a mechanism where the outside shear layer between the atomizing and quiescent air has eddies with associated time scales that increase downstream. At low momentum ratios, the overall droplet time scales are similar to those of the eddies, and droplets interact most with eddies with similar time scales,

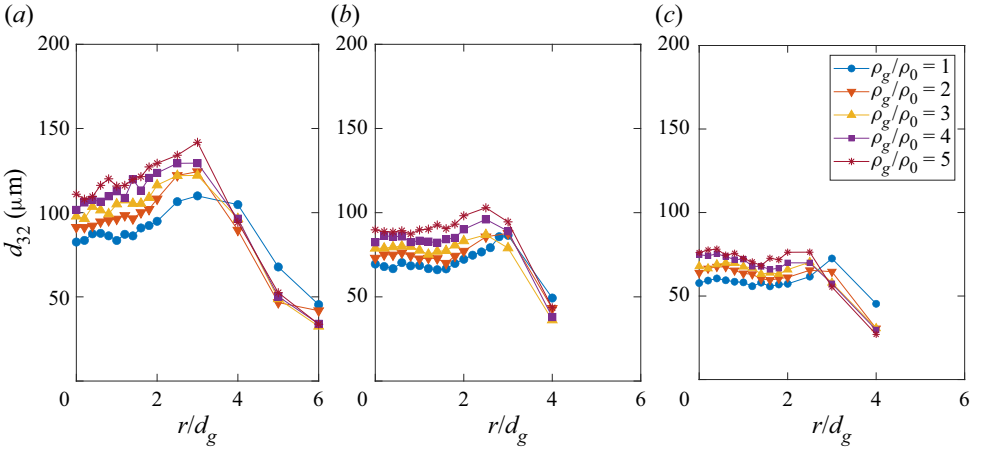

Figure 13. Radial profiles of the Sauter mean droplet diameter d_{32} for the three momentum ratios: (*a*) $M = 25$, (*b*) $M = 39$, and (*c*) $M = 56$. Symbols indicate different air density ratios corresponding to the legend shown in (*c*).

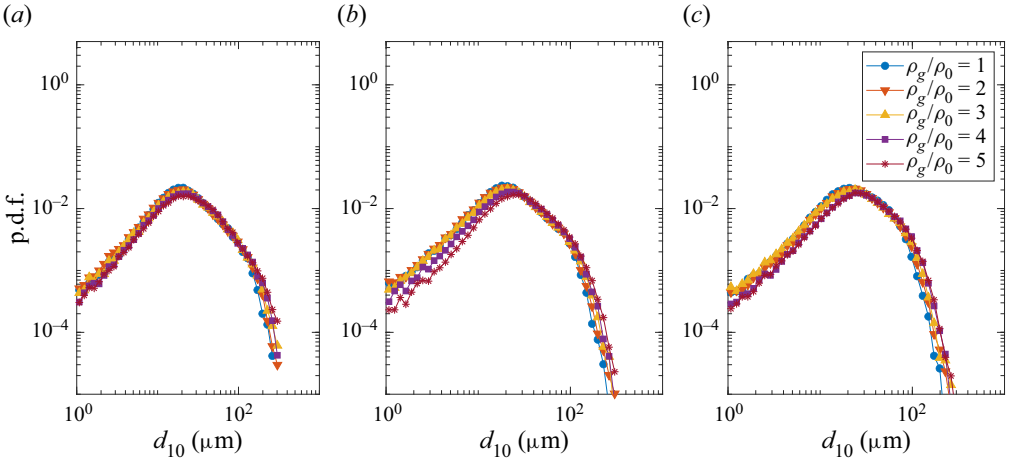

Figure 14. Probability distribution functions (p.d.f.s) of the arithmetic mean droplet diameter d_{10} sampled at the centre of the jet, for the three momentum ratios: (*a*) $M = 25$, (*b*) $M = 39$, and (*c*) $M = 56$. Symbols indicate different air density ratios corresponding to the legend in (*c*).

thus larger droplets reside preferentially towards the outskirts of the spray. However, at momentum ratios beyond the critical value M_C, the droplet time scales are smaller than those of the eddies. Only the smallest droplets are transported by the eddies, whereas larger droplets reside within the inner regions of the spray. This is shown in figure 14, where the probability distribution functions (p.d.f.s) of the droplet diameters at the centre are plotted, showing an increase in the probability of larger droplets as the momentum ratio M increases. These p.d.f.s also show that as the air density increases, the probability of small droplets decreases and the probability of large droplets increases, hence increasing the mean droplet diameters as seen earlier, in figures 12 and 13.

For the same momentum ratio, a clear trend can be observed in figures 12 and 13, where the mean droplet diameters become larger as the air density increases. The increase in

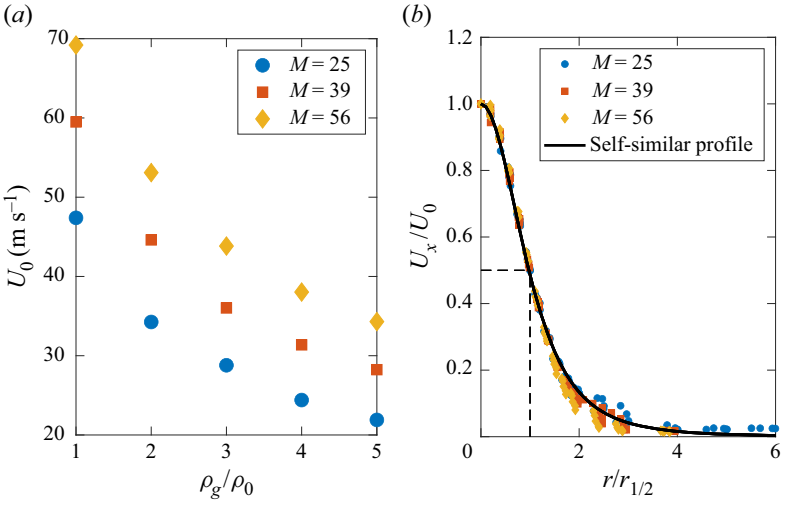

Figure 15. (*a*) Mean droplet axial velocity at the spray centre, U_0, as a function of air density ratio ρ_g/ρ_0. (*b*) Radial profiles of the mean droplet axial velocity, U_x, normalized by their respective centreline velocities U_0, including all M and ρ_g/ρ_0 data, and compared with the self-similarity solution for a free jet. Symbols indicate different momentum ratios, as indicated by the legends.

mean droplet diameters is largely monotonic, and retains similar profile shapes for different air densities, indicating that the critical momentum ratio M_C is independent of the air density. It is also observed that as the sampling locations move away from the spray centre, the mean diameter generally has a maximum at a certain radial distance and then drops towards the edges. This is understood to be the effect of confinement due to the facility, where the mean droplet diameters at the far radial distances are skewed by small recirculating droplets such that the statistical average diameters at the edges always appear to be smaller than the spray characteristics would predict.

4.3. *Droplet and gas phases velocity profiles*

In this experiment, the parameter space is defined by the momentum ratio M as well as the air density ratio ρ_g/ρ_0. Since the liquid flow rate is kept constant throughout the experiment, an increase in ρ_g/ρ_0 results in a decrease in the gas velocity so that the momentum ratio is preserved. Thus the mean droplet axial velocity at the spray centreline, U_0, is shown to decrease with increased air density for the same momentum ratio M, as shown in figure 15(*a*). Nevertheless, regardless of the momentum ratio or air density, the droplet axial velocity profiles all collapse when normalized by their respective half-width $r_{1/2} = r$ ($U_x = 0.5U_0$) in the abscissa, and also by their respective centreline velocities U_0 in the ordinate, as shown in figure 15(*b*). We note that for all cases, the droplet axial velocities are reduced to half the centreline velocity U_0 at a radial position $r = d_g$, meaning that $r_{1/2} \approx d_g$ for all cases, as shown by the dashed lines in figure 15(*b*). These profiles are also shown to match the jet self-similar solution $f(r/r_{1/2}) = (1 + 47S(r/r_{1/2})^2)^{-2}$ (Pope 2000), where $S = 0.094$ is the spreading rate derived by Huck *et al.* (2022) for a two-fluid coaxial jet. Overall, at axial distance $x = 9d_g$ downstream of the nozzle, the droplet axial velocity profiles can be considered fully developed.

While the droplet axial velocities exhibit a canonical profile that is similar across different momentum ratios and air densities, the radial velocity features interesting

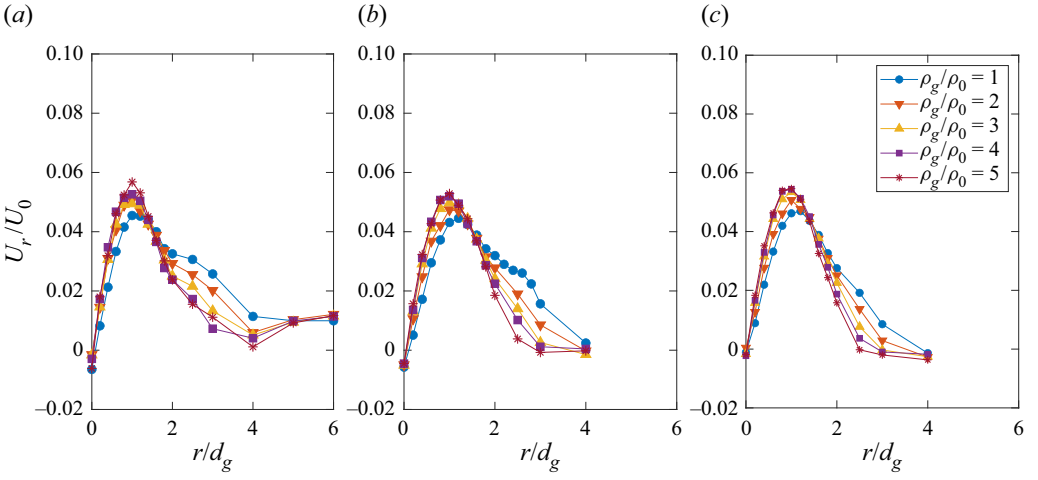

Figure 16. Radial profiles of the mean droplet radial velocity U_r normalized by their respective centreline velocities U_0, for the three momentum ratios: (*a*) $M = 25$, (*b*) $M = 39$, and (*c*) $M = 56$. Symbols indicate different air density ratios corresponding to the legend in (*c*).

dynamics, as shown in figure 16. Across different momentum ratios and air densities, the droplet radial velocity profiles U_r show a maximum mean radial velocity approximately 5 % of the axial centreline velocity, with the maximum value being slightly larger for higher air density cases. This suggests that high air densities act to enhance momentum transfer from the gas to the liquid near the spray centreline, in agreement with prior near-field observations. The opposite trend is shown for far radial distances, where higher air densities yield lower radial velocities for droplets in far radial positions. This can be attributed to the droplets experiencing greater drag when travelling radially through denser air at higher air densities, hence reducing the mean radial velocities of the droplets as they cross the region of zero radial velocity in the gas jet.

Simultaneous measurements of the droplet sizes and axial velocities enabled by the LDV/PDI system also allow for characterization of the axial gas velocity U_{air} for each radial location in the jet, taking the mean axial velocity of all droplets with diameters below 2 µm at that radial location. By taking the resulting mean axial gas velocity and subtracting it from the mean axial velocity of all droplets (i.e. U_x), we obtain a mean slip velocity $U_{slip} = U_x - U_{air}$. Repeating this procedure for different radial locations yields the slip velocity profiles shown in figure 17. As with the radial velocity profiles, the slip velocity profiles are similar across different M and ρ_g/ρ_0 conditions. Near the centre of the spray, the negative value of U_{slip} indicates that the droplet velocities are slower than those of the gas phase. At larger radial distances beyond $r = 0.5d_g$, slip velocities are positive, indicating that droplets travel faster than the gas phase, with maximum slip velocities observed in the region $r \sim 2d_g$ for all cases. This can be interpreted as high-momentum droplets retaining their velocity through the slow-moving gas phase, leading to high slip. We note that the slip velocity profiles are normalized by the droplet velocity at the centre, U_0, for each case. The droplet slip velocity values are higher for low P, as shown in figure 16(*a*). This has implications for the estimation of key dimensionless parameters such as the droplet Reynolds numbers Re_p and the droplet Weber numbers We_p, which we will explore in the next subsection.

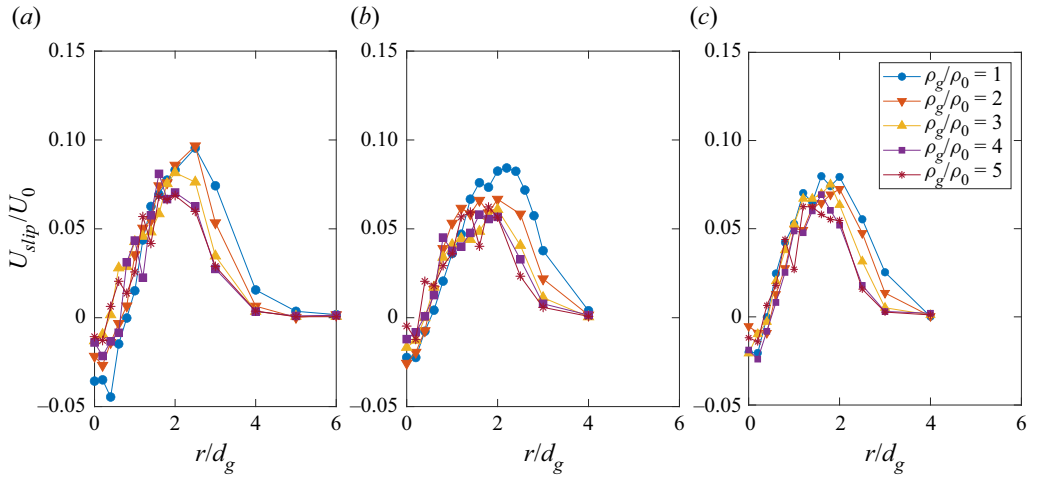

Figure 17. Radial profiles of the mean slip velocity $U_{slip} = U_x - U_{air}$, normalized by their respective centreline droplet velocities U_0, for the three momentum ratios: (*a*) $M = 25$, (*b*) $M = 39$, and (*c*) $M = 56$. Symbols indicate different air density ratios corresponding to the legend shown in (*c*).

4.4. *Role of dimensionless numbers in the droplet size increase with higher air densities*

In this subsection, we present droplet statistics in terms of droplet Reynolds and Weber numbers to analyse potential mechanisms that explain the increase in droplet sizes with ambient pressures (hence air densities), in terms of secondary breakup and transport within the spray. Several important caveats are highlighted here: while the diameter and velocity of each droplet are measured, the gas velocity is known only in an averaged sense (over a period of time where many small droplets cross the LDV/PDI probe volume). Therefore, the corresponding Re_p is also known only in a time-averaged sense. Furthermore, we limit our analysis to droplets from the centre of the spray ($r = 0$) to minimize the effect of not including radial velocities in this analysis (due to the lower data rate in the measurements of this velocity component). With all these considerations, a droplet Reynolds number $Re_p = \rho_g d_d U_{slip}/\mu_g$ can be defined for each droplet, and the p.d.f.s for Re_p are shown in figure 18 for all cases across different M and ρ_g/ρ_0 conditions.

The first observation is that the distribution of Re_p appears to have similar ranges across different M and ρ_g/ρ_0, with a maximum Re_p of ~ 500. Low Re_p droplets are three to four orders of magnitude more probable than high Re_p droplets. The probability of high Re_p droplets increases with increasing air density, and this trend is more apparent in the high momentum ratio cases (figures 18*b*,*c*). This is despite the lower values of the droplet centreline velocity U_0 (and their slip velocities U_{slip}) for droplets in the high ambient air pressure environment. Overall, the majority of droplets have low slip velocity and Re_p, with only a small percentage of droplets reaching high values of Re_p. However, the fraction of droplets with high Re_p increases as the ambient air density increases.

A similar analysis is done with the droplet Weber number $We_p = \rho_g d_d U_{slip}^2/\sigma$, another non-dimensional parameter that influences the droplet breakup process. Figure 19 shows the p.d.f.s of the droplet Weber number, for all cases across different M and ρ_g/ρ_0 conditions. Notably, despite the wide range of Re_p exhibited, the We_p values are small and often less than 3, corresponding to stable droplet sizes in which no secondary breakup occurs (Michaelides *et al.* 2016; Chen *et al.* 2017). Comparing the statistics between the droplet Reynolds and Weber numbers, it is now apparent that the latter is a more

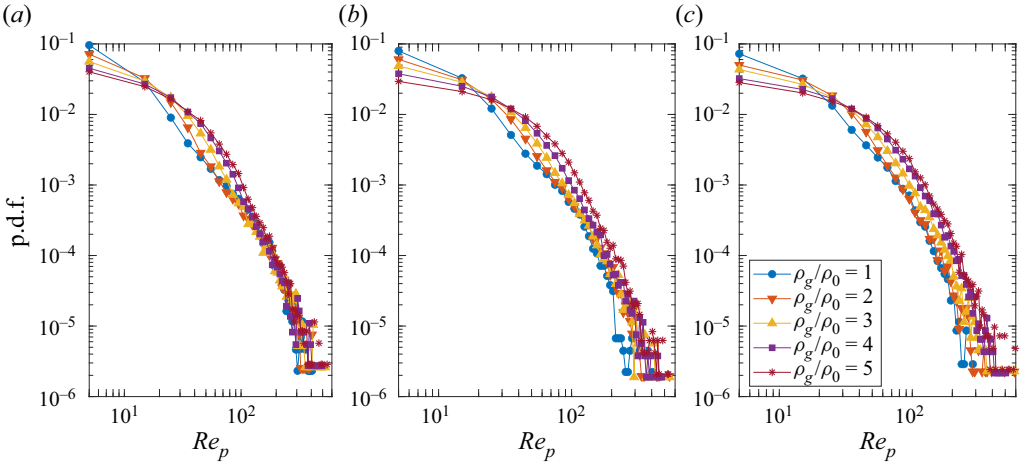

Figure 18. P.d.f.s of the droplet Reynolds number Re_p for droplets sampled at $x = 9d_g$, $r = 0$, for the three momentum ratios: (*a*) $M = 25$, (*b*) $M = 39$, and (*c*) $M = 56$. Symbols indicate different air density ratios corresponding to the legend shown in (*c*).

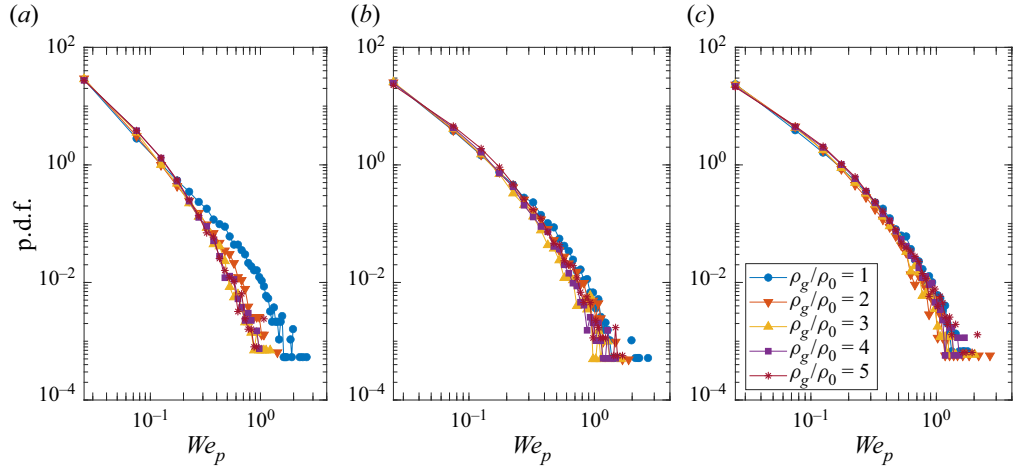

Figure 19. P.d.f.s of the droplet Weber number We_p for droplets sampled at $x = 9d_g$, $r = 0$, for the three momentum ratios: (*a*) $M = 25$, (*b*) $M = 39$, and (*c*) $M = 56$. Symbols indicate different air density ratios corresponding to the legend shown in (*c*).

important parameter with regard to secondary breakup, as shown e.g. by the collapse of the p.d.f.s for the different ambient air pressures, especially for the higher momentum ratios as shown in figures 19(*b*,*c*). The fact that We_p is the dominant parameter that controls droplet fragmentation and the final droplet size also explains our prior observation of larger mean droplet diameters with higher ambient pressures (figures 12 and 13). In general, droplets undergo fragmentation until their sizes are stable (i.e. $We_p = \rho_g d_d U_{slip}^2/\sigma \leq 4$). In a high-pressure environment, the maximum stable droplet size d_d^* is now larger due to the droplet slip velocities U_{slip} being smaller (when the momentum ratio M is constant), and is reflected in the average values of the arithmetic mean and Sauter droplet diameters.

In summary, for the same momentum ratio, higher ambient air pressures (i.e. densities) result in larger droplets in the spray.

4.5. *Liquid recovery rates and momentum transfer between phases*

All prior results and analysis shown are essentially droplet characteristics and their dependency on M, ρ_g/ρ_0 and r. In this subsection, we aim to provide an integral description of the spray, including the net momentum transfer between the gas and liquid phases. To this end, several quantities have to be known, including the total liquid volume flow rate Q_l (from which the percentage recovery rate can be inferred) and the total momentum of the liquid phase $\dot{M}_{l,out}$ (from which the momentum gain in the liquid phase can be computed).

First, an estimation of the probe area is needed. Figure 11 shows a laser collimating lens with focal length $f_c = 750\,\text{mm}$ used on the transmitter, and an imaging lens with $f_i = 250\,\text{mm}$ on the receiver. With this set-up, the probe cross-sectional area (where droplets are detected as they flow through) can be approximated by a rectangle defined as $A = lw$, where $l = s/(\sin(\theta)(f_i/f_c))$ is the probe volume length, as seen from the receiver, truncated by a spatial filter in the receiver ($s = 150\,\mu\text{m}$) and offset at angle $\theta = 30^\circ$. The beam width w is dependent on the diameter of the droplet in the probe volume at each measurement. For each droplet, the product of its residence time (or gate time) in the probe volume and its axial velocity is a path length l that is dependent on the droplet diameter. Then the diameter-dependent beam width w can be estimated by averaging the droplet path lengths conditioned by sizes (e.g. $50 < d_d < 75\,\mu\text{m}$); in our analysis, we group the droplets into 10 equally spaced bins. Finally, the probe area $A_i = dw_i$, dependent on droplet diameter, can be computed. Implementing this procedure corrects a bias that arises from the Gaussian nature of the laser beam causing smaller droplets to be less detectable at the edges of the probe volume (as they scatter less light) than large droplets (Albrecht *et al.* 2013).

Following Huck *et al.* (2022), the volume flux of liquid calculated for each diameter bin i, containing a total number N_i of droplets, is given by

$$\dot{G}(d_i) = \frac{1}{T_s A_i} \sum_{j=1}^{N_i} \frac{d_{j,i}^3}{6}, \tag{4.2}$$

where subscript i refers to the diameter bins, and j to the total number of droplets in the ith diameter bin. Here, T_s is the total sample time, and A_i is the probe cross-section for droplets corresponding to the ith diameter bin. Integrating over all D droplet size bins ($D = 10$ in our analysis) yields $\dot{g}(r)$, the actual volume flux of liquid passing through each location sampled in the spray:

$$\dot{g}(r) = \sum_{i=1}^{D} \dot{G}(d_i). \tag{4.3}$$

The radial profiles of $\dot{g}(r)$ are plotted in figure 20 for all cases across different M and ρ_g/ρ_0. For the same momentum ratio M, the profiles of $\dot{g}(r)$ appear similar across different air density ratios ρ_g/ρ_0, and $\dot{g}(r)$ increases with M, indicating that more liquid passes through the probe location per unit time.

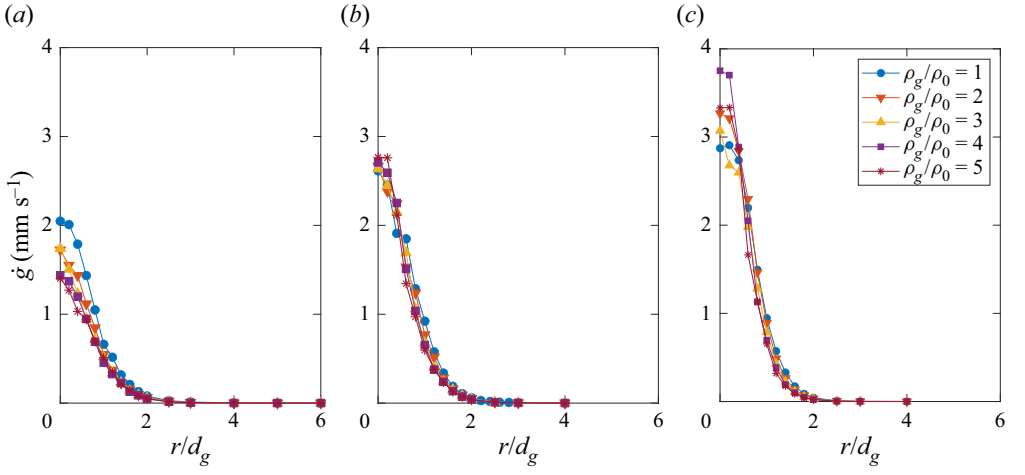

Figure 20. Radial profiles of the liquid volume flux $\dot{g}$ at the sampling location for the three momentum ratios: (*a*) $M = 25$, (*b*) $M = 39$, and (*c*) $M = 56$. Symbols indicate different air density ratios corresponding to the legend shown in (*c*).

Similar to $\dot{g}(r)$, the momentum flux of liquid passing through the measuring point, $\dot{m}_l(r)$, can be computed by

$$\dot{\mathcal{M}}_l(d_i) = \frac{1}{T_s A_i} \sum_{j=1}^{N_i} \frac{1}{6} \rho_l U_{j,i} d_{j,i}^3, \tag{4.4}$$

$$\dot{m}_l(r) = \sum_{i=1}^{D} \dot{\mathcal{M}}_l(d_i). \tag{4.5}$$

Profiles of $\dot{m}_l(r)$ are plotted in figure 21 for all M and ρ_g/ρ_0. Across all cases, the profiles generally feature lower momentum flux with higher air densities.

Integrating the profiles in figure 20 yields the total liquid volume flow rate $Q_l = \int_0^R 2\pi r\, \dot{g}(r)\, \mathrm{d}r$. This in turn can be used as a measure of the recovery rate by dividing Q_l by the input volume flow rate $Q_{l,in} = 1650\,\mathrm{mm^3\,s^{-1}}$, resulting in recovery values in the range from 28 % to 53 % of the liquid injected, as shown in figure 22(*a*); i.e. not every droplet passing through the PDI probe volume is captured. Similarly, the total momentum in the liquid phase can also be integrated from the radial profiles in figure 21 as $\dot{M}_{l,out} = \int_0^R 2\pi r\, \dot{m}_l(r)\, \mathrm{d}r$. To compute the net momentum gained by the liquid phase in the spray, one divides the previous result by the liquid momentum injected, $\dot{M}_{l,in} = \rho_l U_l^2 A_l$. Figure 22(*b*) shows that for all cases, there is a net momentum gain in the liquid phase that is larger for higher momentum ratios M. This momentum transfer from the gas to the liquid is larger in lower air densities, i.e. for lower ρ_g/ρ_0. This observation holds even when the momentum gain is adjusted to account for the liquid phase recovery rate, as shown in figure 22(*c*), where the overall momentum gain in the liquid phase of a spray atomizer is seen to diminish in an environment with high ambient air pressure (i.e. high air density).

5. Effect of varying air densities on instabilities causing the atomization process

As discussed in the Introduction, the atomization process is the combination of the primary Kelvin–Helmholtz (K–H) instability, and the secondary Rayleigh–Taylor instability at high

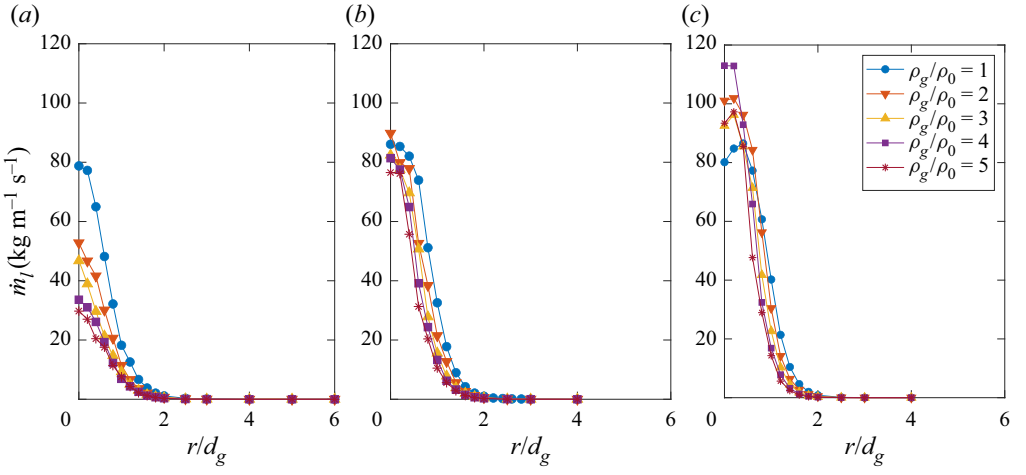

Figure 21. Radial profiles of the liquid momentum flux $\dot{m}_l$ at the sampling location for the three momentum ratios: (*a*) $M = 25$, (*b*) $M = 39$, and (*c*) $M = 56$. Symbols indicate different air density ratios corresponding to the legend shown in (*c*).

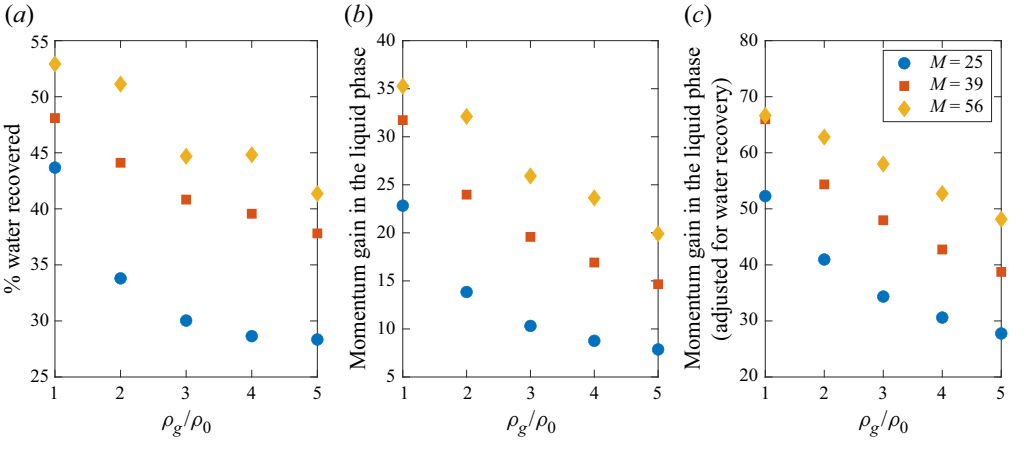

Figure 22. (*a*) Liquid recovery from the LDV/PDI measurements. (*b*) Momentum gain in the liquid phase. (*c*) Momentum gain after adjusting for the liquid recovery. Symbols indicate different momentum ratios, and the *x*-axis shows different air densities.

jet Weber numbers. The modulation of the atomized spray behaviour with increased air density can be shown as a direct result of changes in instability wavelengths and growth rates due to the higher gas densities. Considering first the primary K–H instability, it can be characterized by a growth rate n associated with a wavenumber k as follows (Ng 2015):

$$n(k) = \frac{k}{\rho_l + \rho_g}\sqrt{\rho_l\rho_g(U_g - U_l)^2 - (\rho_l + \rho_g)\sigma k}, \tag{5.1}$$

for which the plot in figure 23(*a*) shows the relationship between n and k, using gas and liquid velocities and densities for case $M = 25$ and $\rho_g/\rho_0 = 1$. From (5.1), the wavenumber of maximum growth $k_{max,KH}$ can be approximated by taking $U_g \gg U_l$ and $\rho_l \gg \rho_g$, and solving $\mathrm{d}n/\mathrm{d}k = 0$, resulting in $k_{max,KH} \sim 2\rho_g U_g^2/3\sigma$, which is represented

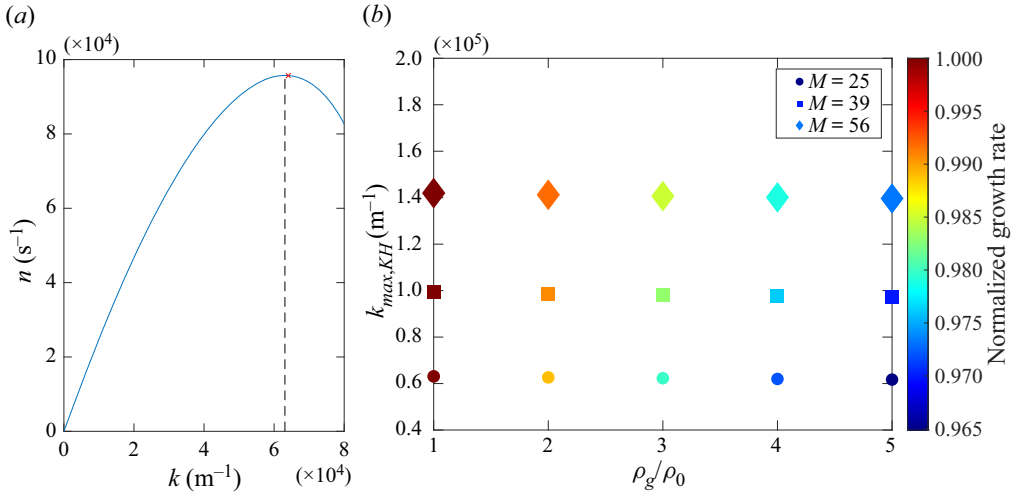

Figure 23. (*a*) Instability wavenumber k and its associated growth rate n for $M = 25$ and $\rho_g/\rho_0 = 1$. The black dashed line indicates the wavenumber with the highest growth rate $k_{max,KH}$, and the red cross indicates the growth rate for the instability with wavenumber $k = 2\rho_g U_g^2/3\sigma$. (*b*) Wavenumber associated with the maximum growth rate $k_{max,KH}$ for different momentum ratios and different air densities. Symbol sizes indicate the relative magnitudes of the growth rate n. Symbol colours indicate the value of the growth rate normalized by the maximum growth rate for each momentum ratio at $\rho_g/\rho_0 = 1$.

as a red cross in figure 23(*a*), and is shown to approximate closely the actual value of $k_{max,KH}$ represented by the dashed vertical line.

For different momentum and ambient air pressures, (5.1) shows the dependence of the growth rate n on the gas velocity, and more importantly the gas density, compared to the wavenumber of maximum growth $k_{max,KH}$, which is less dependent on the gas density. Indeed, by calculating $n(k)$ for $M = 25, 39, 56$ and $\rho_g/\rho_0 = 1$–5, and plotting the value of $k_{max,KH}$ as shown in figure 23(*b*), it is shown that the values of $k_{max,KH}$ are larger with increased momentum ratio M, due to the dependence of k on the gas velocity. Larger wavenumbers correspond to smaller K–H perturbation wavelengths, which is represented in the macro-scale as a narrowing of the spray with higher momentum ratios, a well-known result observed by Lasheras *et al.* (1998) and Machicoane *et al.* (2020), among others.

In contrast, the effect of increased ambient pressure, and hence increased air density, on the growth rate n is more subtle. In figure 23(*b*), for each momentum ratio M, the growth rate is largest at $\rho_g/\rho_0 = 1$, and decreases progressively as ρ_g/ρ_0 increases, represented through the colour of the data points normalized by the maximum growth rate at $\rho_g/\rho_0 = 1$. This reduction in the K–H instability growth rate correlates well with our near-field observations using shadowgraphy, in which for constant M, higher air densities result in a narrowing of the spray spreading angle (figure 8) as well as a longer mean liquid core length (figure 6). While the K–H instability framework does not take into account viscosity effects (Matas 2015), the global effect on macro-scale spray metrics such as the spreading angle and liquid core length are well captured, even without including the discussion of gas viscosity impact on the boundary layer and its influence on the K–H instability of the liquid column. This analysis also does not apply to low Weber-number jets (corresponding to our $M = 5$ case), where the flapping instability dominates (Matas & Cartellier 2006).

Whereas the K–H instability dominates the initial breakup of the liquid column, the formation of ligaments observed by Marmottant & Villermaux (2004), and the subsequent

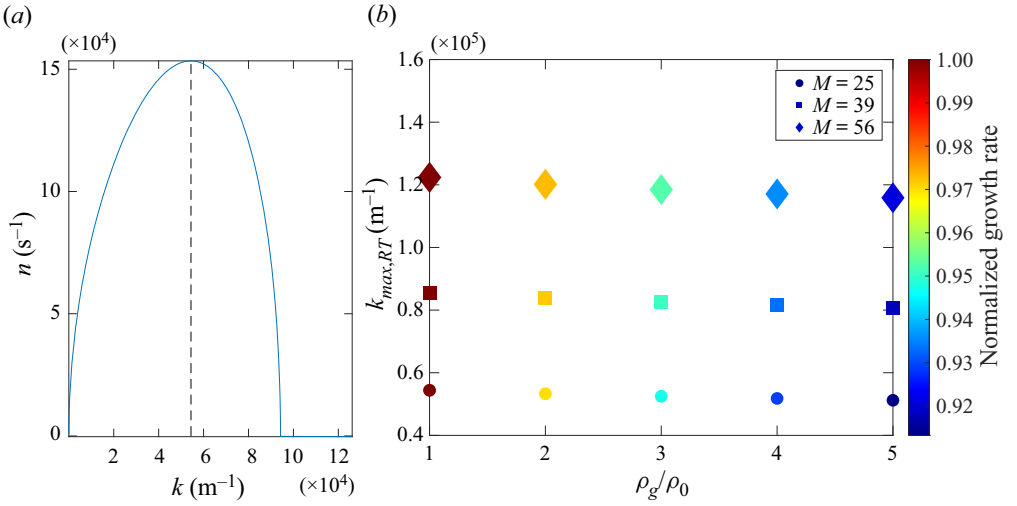

Figure 24. (*a*) Instability wavenumber k and its associated growth rate n for the case $M = 25$ and $\rho_g/\rho_0 = 1$. The black dashed line indicates the wavenumber with the highest growth rate. (*b*) Wavenumber associated with maximum growth rate, $k_{max,KH}$ for different momentum ratios (indicated by different symbols) and different air densities. Symbol sizes indicate the relative magnitudes of the growth rate n. Symbol colours indicate the value of the growth rate normalized by the maximum growth rate for each momentum ratio at $\rho_g/\rho_0 = 1$.

breakup into droplets, hints that a secondary instability process is at play. As discussed previously, this is the Rayleigh–Taylor instability that becomes relevant at large jet Weber numbers ($We > 100$), and is studied by Aliseda *et al.* (2008), who derived instability relations similar to those for the K–H instability:

$$n(k) = \frac{-k^2\mu_l}{\rho_l} \pm \sqrt{\frac{k^4\mu_l^2}{\rho_l^2} - \frac{k^3\sigma}{\rho_l} + ka}, \tag{5.2}$$

where k is the instability wavenumber, and n is its associated growth rate. Here, a is an acceleration term defined by

$$a \approx \frac{10\rho_g(U_g - U_c)^2}{\rho_l \lambda_{KH}}, \tag{5.3}$$

where λ_{KH} is the wavelength associated with $k_{max,KH}$, and U_c is the velocity of the ligaments formed from the K–H instability (Dimotakis 1986; Aliseda *et al.* 2008) and defined as

$$U_c = \frac{\sqrt{\rho_l}\,U_l + \sqrt{\rho_g}\,U_g}{\sqrt{\rho_l} + \sqrt{\rho_g}}. \tag{5.4}$$

Together, these allow us to compute the relation between n and k defined in (5.2) (figure 24*a*), and derive a wavenumber of maximum growth $k_{max,RT}$ and a corresponding growth rate for different momentum ratios and air densities (figure 24*b*). For the different air densities, the value of $k_{max,RT}$ is still dominated largely by the momentum ratio M, with larger values of $k_{max,RT}$ corresponding to smaller perturbation wavelengths, resulting ultimately in smaller droplets formed from the ligament breakup. However, there is also a small but non-negligible decrease in $k_{max,RT}$ when ρ_g/ρ_0 increases. In addition, similar to results seen in the K–H analysis, the growth rates n of the Rayleigh–Taylor instability tend to decrease with increasing ρ_g/ρ_0.

Both trends observed in n and k in the Rayleigh–Taylor instability analysis point towards a tendency for ligament breakup into larger droplets in the presence of higher ambient air pressures/densities. This is in tandem with the other analysis shown in § 4.4, in which the existence of larger droplets is attributed to the lower slip velocities U_{slip} resulting in droplet Weber numbers that lie below the critical value for fragmentation. In other words, for the same M, increasing ρ_g/ρ_0 not only favours larger droplets due to their lower slip velocities, but also modulates the upstream ligament breakup process to favour formation of larger droplets (figures 12 and 13).

6. Conclusions

We report on a series of experiments on gas–liquid atomization in a novel setting where the atomized spray is formed in a pressurized environment. The pressurized ambient air means that the surrounding air density is higher compared to standard conditions, thereby affecting not only the atomization process but also the resulting droplet sizes and velocities in the spray. Using high-speed shadowgraphy, it is shown that the macroscopic features of the spray are modulated by the higher air densities, including a reduction in spray spreading angle and elongation of the mean intact liquid core length. A power spectral density analysis performed on the time-resolved spray images also reveals that characteristic frequencies of the spray are shifted to higher frequencies when the air density is increased. Taken together, these observations suggest that for the same momentum ratio M but at increased air density ratios ρ_g/ρ_0, the momentum transfer from the gas phase to the liquid phase is enhanced in the near-field.

For measurements conducted in the mid-field ($x = 9d_g$ downstream), the most striking observation is that elevated ambient and co-flowing air densities lead to the formation of larger droplets, as inferred from data collected on diameters and velocities of individual droplets using a point-measurement LDV/PDI system. As the momentum ratio M is conserved when the air density changes, the lower absolute slip velocities U_{slip} experienced by the droplets favours stable larger droplets as reflected in the lower droplet Weber numbers. The higher air densities also favour initial formation of larger droplets in the near-field through a modulation of the Rayleigh–Taylor instability, the combined effect being an overall increase in droplet diameters. However, regimes of spray behaviour demarcated by the critical momentum ratio M_C, such as the radial variation of mean droplet diameters, are shown to not be influenced by the change in air density. The higher air densities are also shown to decrease the net momentum transfer between the gas and liquid phases. This can be explained by the formation of larger droplets, which also results in higher droplet Reynolds numbers, returning momentum to the gas phase in the mid-field, through enhanced drag forces. Indeed, integrated results shown in figure 22 show that in the mid-field, the net momentum gain in the liquid phase is diminished by up to 50 % when the air density ratio ρ_g/ρ_0 increases from 1 to 5, as shown for all momentum ratios.

Several key observations here deserve emphasis. In the gas–liquid coaxial atomization system, the momentum ratio M is shown to prevail as the most relevant parameter even in the scenario of varying ambient pressures/air densities, whereas at the droplet scale, the droplet Weber number We_p is shown to be more influential to droplet formation and sizing, compared to the droplet Reynolds number Re_p. The key here is that both M and We_p are quantities that depend on the square of the velocity, or U^2, which is also featured in the underlying instabilities that govern the spray atomization process. Indeed, the growth rates of the Kelvin–Helmholtz and Rayleigh–Taylor instabilities ((5.1) and (5.2)) show scaling

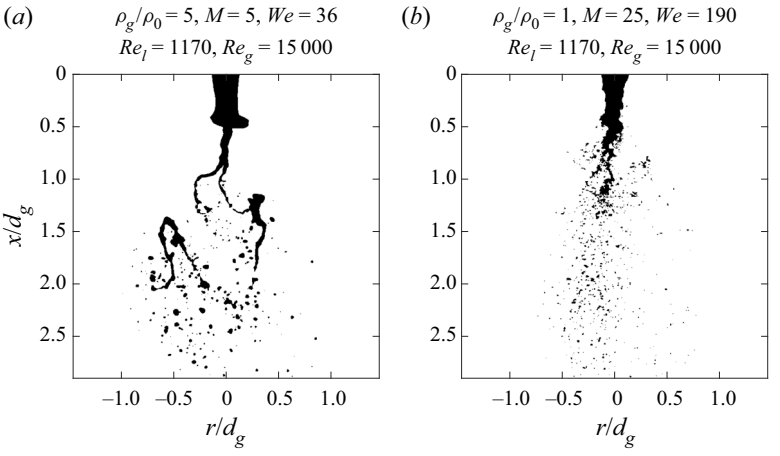

Figure 25. Instantaneous binarized spray images comparing two cases with the same gas and liquid Reynolds numbers ($Re_l = 1170$, $Re_g = 15\,000$), but different momentum ratios ($M = 5, 25$) and liquid Weber numbers ($We = 36, 190$).

with the squared velocity as well. In short, spray atomization and liquid fragmentation are processes that scale with $\sim U^2$, and can be characterized fully by dimensionless parameters with U^2 terms, such as the momentum ratio $M = \rho_g U_g^2/\rho_l U_l^2$ or the liquid Weber number $We = \rho_g(U_g - U_l)^2 d_l/\sigma$, even in the case of varying ambient air pressures and hence air densities. This is illustrated clearly in figure 25, where two sprays with the same gas and liquid Reynolds numbers, but very different in momentum ratios and liquid Weber numbers, feature very different spray behaviours in the near-field of the spray. These findings also carry important implications for real-time spray control in environments with varying pressures. For example, an increase in ambient pressures will result in a deviation from an optimum spray spreading angle. In conditions where the momentum ratio needs to stay constant (e.g. limited atomizing air flow rates, or fixed stoichiometry requirements), recovery of the spreading angle can be achieved by adding swirl into the gas flow (Machicoane *et al.* 2020). Alternatively, one can employ electrostatic fields around the spray (Osuna-Orozco *et al.* 2020), which not only increases the spray spreading angle, but also favours the formation of smaller droplets, which also counters the effect of elevated gas pressures/densities increasing the size of droplets. Together, the spray control tools of swirl and electrostatic fields can act to compensate the effects of pressurization and maintain an optimum spray configuration and atomized droplet size distribution.

In comparison, the Reynolds number of the droplets does not play a strong role in characterizing the atomization process, but it is important in mediating the momentum transfer between the gas and liquid phases. In the presence of higher ambient air pressures/densities, the resulting decrease in momentum gain (figure 22*c*) of the liquid phase may have considerable impact on its far-field ($x \gg 9d_g$) dispersion, such as in a turbulent environment (Carter *et al.* 2020). This reduction in far-field dispersion may be mitigated by increasing the jet momentum ratio, while employing simultaneously swirl and electrostatic controls to maintain the same spray spreading angle, as mentioned earlier. In view of the importance of the far-field dispersion of the liquid phase to reaction processes, further investigations in the far-field regions of the atomized spray are warranted to study how ambient air pressurization modulates the gas–liquid momentum transfer process and the dispersion of the liquid phase. However, one should also bear in mind

that the far-field dispersion of the atomized liquid droplets is also dependent on the initial upstream atomization process. This can be alleviated partially with high-fidelity simulations, where elevated gas densities reduce the gas–liquid density ratio (ρ_l/ρ_g) from $O(10^3)$ to $O(10^2)$, making it more computationally tractable for complete atomization simulations from primary atomization to droplet secondary breakup and transport (Ling, Zaleski & Scardovelli 2015). On the other hand, for experiments in the field of engine research, practical considerations usually leads to fuel or air injection pressures being fixed in experiments such as those performed by Naber & Siebers (1996), which keeps the ratio between gas and liquid Reynolds numbers constant, but increases M when the ambient air pressure is increased. While both choices are acceptable, representing different stages of the atomization process, future research should strive to incorporate both aspects to facilitate improved understanding of the coaxial atomization process.

Acknowledgements. The authors thank our collaborators T. Heindel and his group at Iowa State University, USA, for their assistance in constructing the experimental facility.

Funding. This work was sponsored by the United States Office of Naval Research (ONR), as part of the Multidisciplinary University Research Initiatives (MURI) Program, under grant no. N00014-16-1-2617.

Declaration of interests. The authors report no conflict of interest.

Author ORCIDs.
Kee Onn Fong https://orcid.org/0000-0002-6356-356X;
Xinzhi Xue https://orcid.org/0000-0003-2892-5112;
R. Osuna-Orozco https://orcid.org/0000-0002-4952-2470;
A. Aliseda https://orcid.org/0000-0002-5832-2999.

References

Albrecht, H.-E., Damaschke, N., Borys, M. & Tropea, C. 2013 *Laser Doppler and Phase Doppler Measurement Techniques*. Springer Science & Business Media.

Aliseda, A., Hopfinger, E.J., Lasheras, J.C., Kremer, D.M., Berchielli, A. & Connolly, E.K. 2008 Atomization of viscous and non-Newtonian liquids by a coaxial, high-speed gas jet, experiments and droplet size modeling. *Intl J. Multiphase Flow* **34** (2), 161–175.

Apte, S.V., Mahesh, K., Moin, P. & Oefelein, J.C. 2003 Large-eddy simulation of swirling particle-laden flows in a coaxial-jet combustor. *Intl J. Multiphase Flow* **29** (8), 1311–1331.

Bendat, J.S. & Piersol, A.G. 2011 *Random Data: Analysis and Measurement Procedures*. John Wiley & Sons.

Bozonnet, C., Matas, J.-P., Balarac, G. & Desjardins, O. 2022 Stability of an air–water mixing layer: focus on the confinement effect. *J. Fluid Mech.* **933**, A14.

Burtnett, T., Morgan, T., Dahlstrom, T., Aliseda, A. & Heindel, T. 2021 A pressurized tank for high flow rate atomization studies. In *International Conference on Liquid Atomization and Spray Systems (ICLASS)*, vol. 1.

Carter, D.W., Hassaini, R., Eshraghi, J., Vlachos, P. & Coletti, F. 2020 Multi-scale imaging of upward liquid spray in the far-field region. *Intl J. Multiphase Flow* **132**, 103430.

Chen, Y., *et al.* 2017 Aerodynamic breakup and secondary drop formation for a liquid metal column in a shock-induced cross-flow. In *55th AIAA Aerospace Sciences Meeting, AIAA Paper* 2017-1892.

Chigier, N. & Farago, Z. 1992 Morphological classification of disintegration of round liquid jets in a coaxial air stream. *Atomiz. Sprays* **2** (2), 137–153.

Chigier, N. & Reitz, R.D. 1996 Regimes of jet breakup and breakup mechanisms – physical aspects. In *Recent Advances in Spray Combustion: Spray Atomization and Drop Burning Phenomena* (ed. K.K. Kuo), vol. 1, pp. 109–135. AIAA.

Delon, A., Cartellier, A. & Matas, J.-P. 2018 Flapping instability of a liquid jet. *Phys. Rev. Fluids* **3** (4), 043901.

Dimotakis, P.E. 1986 Two-dimensional shear-layer entrainment. *AIAA J.* **24** (11), 1791–1796.

Eggers, J. & Villermaux, E. 2008 Physics of liquid jets. *Rep. Prog. Phys.* **71** (3), 036601.

EROGLU, H., CHIGIER, N. & FARAGO, Z. 1991 Coaxial atomizer liquid intact lengths. *Phys. Fluids* A **3** (2), 303–308.

FANSLER, T.D. & PARRISH, S.E. 2014 Spray measurement technology: a review. *Meas. Sci. Technol.* **26** (1), 012002.

GOROKHOVSKI, M. & HERRMANN, M. 2008 Modeling primary atomization. *Annu. Rev. Fluid Mech.* **40**, 343–366.

HOPFINGER, E.J. & LASHERAS, J.C. 1996 Explosive breakup of a liquid jet by a swirling coaxial gas jet. *Phys. Fluids* **8** (7), 1696–1698.

HUCK, P., OSUNA-OROZCO, R., MACHICOANE, N. & ALISEDA, A. 2021 Effects of acoustic actuation on a multi-phase jet. In *15th Triennial International Conference on Liquid Atomization and Spray Systems*.

HUCK, P.D., OSUNA-OROZCO, R., MACHICOANE, N. & ALISEDA, A. 2022 Spray dispersion regimes following atomization in a turbulent co-axial gas jet. *J. Fluid Mech.* **932**, A36.

JIANG, D. & LING, Y. 2021 Impact of inlet gas turbulence on the formation, development and breakup of interfacial waves in a two-phase mixing layer. *J. Fluid Mech.* **921**, A15.

JOSEPH, D.D., BELANGER, J. & BEAVERS, G.S. 1999 Breakup of a liquid drop suddenly exposed to a high-speed airstream. *Intl J. Multiphase Flow* **25** (6–7), 1263–1303.

KASTENGREN, A.L., POWELL, C.F., WANG, Y., IM, K.-S. & WANG, J. 2009 X-ray radiography measurements of diesel spray structure at engine-like ambient density. *Atomiz. Sprays* **19** (11), 1031–1044.

KUNDU, P.K., COHEN, I.M. & DOWLING, D.R. 2015 *Fluid Mechanics*. Academic Press.

LASHERAS, J.C. & HOPFINGER, E.J. 2000 Liquid jet instability and atomization in a coaxial gas stream. *Annu. Rev. Fluid Mech.* **32** (1), 275–308.

LASHERAS, J.C., VILLERMAUX, E. & HOPFINGER, E.J. 1998 Break-up and atomization of a round water jet by a high-speed annular air jet. *J. Fluid Mech.* **357**, 351–379.

LEONG, M.Y., MCDONELL, V.G. & SAMUELSEN, G.S. 2001 Effect of ambient pressure on an airblast spray injected into a crossflow. *J. Propul. Power* **17** (5), 1076–1084.

LING, Y., ZALESKI, S. & SCARDOVELLI, R. 2015 Multiscale simulation of atomization with small droplets represented by a Lagrangian point-particle model. *Intl J. Multiphase Flow* **76**, 122–143.

LIU, K., HUCK, P.D., ALISEDA, A. & BALACHANDAR, S. 2021 Investigation of turbulent inflow specification in Euler–Lagrange simulations of mid-field spray. *Phys. Fluids* **33** (3), 033313.

LO, H.Y., CARROLL, D.L. & STIEL, L.I. 1966 Viscosity of gaseous air at moderate and high pressures. *J. Chem. Engng Data* **11** (4), 540–544.

LUBARSKY, E., REICHEL, J.R., ZINN, B.T. & MCAMIS, R. 2010 Spray in crossflow: dependence on Weber number. *Trans. ASME J. Engng Gas Turbines Power* **132** (2), 021501.

MACHICOANE, N., BOTHELL, J.K., LI, D., MORGAN, T.B., HEINDEL, T.J., KASTENGREN, A.L. & ALISEDA, A. 2019 Synchrotron radiography characterization of the liquid core dynamics in a canonical two-fluid coaxial atomizer. *Intl J. Multiphase Flow* **115**, 1–8.

MACHICOANE, N., RICARD, G., OSUNA-OROZCO, R., HUCK, P.D. & ALISEDA, A. 2020 Influence of steady and oscillating swirl on the near-field spray characteristics in a two-fluid coaxial atomizer. *Intl J. Multiphase Flow* **129**, 103318.

MARMOTTANT, P. & VILLERMAUX, E. 2004 On spray formation. *J. Fluid Mech.* **498**, 73–111.

MATAS, J.-P. 2015 Inviscid versus viscous instability mechanism of an air–water mixing layer. *J. Fluid Mech.* **768**, 375–387.

MATAS, J.-P. & CARTELLIER, A. 2006 Study of the helical instability in the air assisted atomization of a liquid jet. In *10th International Conference on Liquid Atomization and Spray Systems*.

MATAS, J.-P., MARTY, S., DEM, M.S. & CARTELLIER, A. 2015 Influence of gas turbulence on the instability of an air–water mixing layer. *Phys. Rev. Lett.* **115** (7), 074501.

MICHAELIDES, E., CROWE, C.T. & SCHWARZKOPF, J.D. 2016 *Multiphase Flow Handbook*. CRC Press.

NABER, J.D. & SIEBERS, D.L. 1996 Effects of gas density and vaporization on penetration and dispersion of diesel sprays. *SAE Trans.* **105**, 82–111.

NG, C.H. 2015 Experimental studies of the breakup dynamics in turbulent multiphase jets. PhD thesis. University of Washington.

OSUNA-OROZCO, R., MACHICOANE, N., HUCK, P.D. & ALISEDA, A. 2019 Feedback control of coaxial atomization based on the spray liquid distribution. *Atomiz. Sprays* **29** (6), 545–551.

OSUNA-OROZCO, R., MACHICOANE, N., HUCK, P.D. & ALISEDA, A. 2020 Feedback control of the spray liquid distribution of electrostatically assisted coaxial atomization. *Atomiz. Sprays* **30** (1), 1–9.

PICKETT, L.M., GENZALE, C.L., BRUNEAUX, G., MALBEC, L.-M., HERMANT, L., CHRISTIANSEN, C. & SCHRAMM, J. 2010 Comparison of diesel spray combustion in different high-temperature, high-pressure facilities. *SAE Intl J. Engines* **3** (2), 156–181.

PICKETT, L.M., KOOK, S. & WILLIAMS, T.C. 2009 Visualization of diesel spray penetration, cool-flame, ignition, high-temperature combustion, and soot formation using high-speed imaging. *SAE Intl J. Engines* **2** (1), 439–459.

POPE, S.B. 2000 *Turbulent Flows*. Cambridge University Press.

VARGA, C.M., LASHERAS, J.C. & HOPFINGER, E.J. 2003 Initial breakup of a small-diameter liquid jet by a high-speed gas stream. *J. Fluid Mech.* **497**, 405–434.

VARGAFTIK, N.B., VOLKOV, B.N. & VOLJAK, L.D. 1983 International tables of the surface tension of water. *J. Phys. Chem. Ref. Data* **12** (3), 817–820.

VILLERMAUX, E. 2007 Fragmentation. *Annu. Rev. Fluid Mech.* **39**, 419–446.